

The Role of Magnetic Fields in the Formation of the Filamentary Infrared Dark Cloud G11.11–0.12

Zhiwei Chen (陈志维),^{1*} Ramotholo Sefako,² Yang Yang,³ Zhibo Jiang,¹ Yang Su,¹ Shaobo Zhang¹ and Xin Zhou¹

¹*Purple Mountain Observatory, Chinese Academy of Sciences, 10 Yuanhua Road, 210023 Nanjing, China*

²*South African Astronomical Observatory, PO Box 9, Observatory 7935, Cape Town, South Africa*

³*Center for Astrophysics, Guangzhou University, Guangzhou 510006, China*

Accepted 2023 July 21. Received 2023 July 20; in original form 2022 July 06

ABSTRACT

We report on the near-infrared polarimetric observations of G11.11–0.12 (hereafter G11) obtained with SIRPOL on the 1.4 m IRSF telescope. The starlight polarisation of the background stars reveals the on-sky component of magnetic fields in G11, and these are consistent with the field orientation observed from polarised dust emission at 850 μm . The magnetic fields in G11 are perpendicular to the filament, and are independent of the filament’s orientation relative to the Galactic plane. The field strength in the envelope of G11 is in the range 50 – 100 μG , derived from two methods. The analyses of the magnetic fields and gas velocity dispersion indicate that the envelope of G11 is supersonic but sub-Alfvénic. The critical mass-to-flux ratio in the envelope of G11 is close to 1 and increases to ≥ 1 on the spine of G11. The relative weights on the importance of magnetic fields, turbulence and gravity indicate that gravity dominates the dynamical state of G11, but with significant contribution from magnetic fields. The field strength, $|\mathbf{B}|$, increases slower than the gas density, n , from the envelope to the spine of G11, characterized by $|\mathbf{B}| \propto n^{0.3}$. The observed strength and orientation of magnetic fields in G11 imply that supersonic and sub-Alfvénic gas flow is channelled by the strong magnetic fields and is assembled into filaments perpendicular to the magnetic fields. The formation of low-mass stars is enhanced in the filaments with high column density, in agreement with the excess of low-mass protostars detected in the densest regions of G11.

Key words: ISM: clouds – ISM: magnetic fields – ISM: kinematics and dynamics – ISM: individual objects: G11

1 INTRODUCTION

Filaments are ubiquitous interstellar medium (ISM) structures in galaxies. Their formation is, however, still a controversial topic (see André et al. 2014; Hacar et al. 2022, for reviews). Gas compression due to supersonic turbulence and/or colliding gas flow is supposed to be responsible for the formation of filaments (e.g. Vázquez-Semadeni 1994; Padoan et al. 2001; Vázquez-Semadeni et al. 2006; Heitsch et al. 2006). Once a compressed layer more massive than the average Jeans mass is formed, gravitational contraction starts to take control of the evolution, and naturally produce filaments in the cloud and clumps inside the filaments (e.g. Gómez & Vázquez-Semadeni 2014; Naranjo-Romero et al. 2022). The clumps in filaments are potential sites of star formation triggered by gravitational collapse (e.g. Wareing et al. 2019; Yang et al. 2020, 2021). Star formation activity such as in young stellar objects are mostly found in filaments (e.g. Ragan et al. 2012; Zhang et al. 2019). In addition to turbulence and gravity, magnetic field also plays an important role in the formation and evolution of filaments (e.g. Hanawa et al. 1993; Gehman et al. 1996). In the past two decades, magnetohydrodynamic (MHD) simulations and observations of magnetic fields in filaments

have shown that magnetic fields play an important role in shaping filaments and regulating the subsequent star formation inside them (e.g. Goldsmith et al. 2008; Inoue & Inutsuka 2008; Heitsch et al. 2009; Sugitani et al. 2011; Chapman et al. 2011; Hennebelle 2013; Soler et al. 2013; Seifried & Walch 2015; Körtgen & Banerjee 2015; Santos et al. 2016; Zamora-Avilés et al. 2018; Mocz & Burkhardt 2018; Li & Klein 2019; Körtgen & Soler 2020; Arzoumanian et al. 2021; Ibáñez-Mejía et al. 2022; Li et al. 2022).

The orientation of magnetic fields with respect to filaments shows a bimodal distribution, either parallel or perpendicular (e.g. Li et al. 2013; Clark et al. 2014; Li et al. 2014; Planck Collaboration et al. 2016a; Soler et al. 2017; Soler 2019). The bimodal orientation between magnetic fields and filaments is an indication of the physical link between magnetic fields and filaments, otherwise orientation between them should be following a random distribution. A flip in relative orientation, from parallel to perpendicular, occurs around a transition column density of $\sim 10^{21-22} \text{ cm}^{-2}$ (e.g. Chen et al. 2016; Malinen et al. 2016; Planck Collaboration et al. 2016b; Soler et al. 2017; Heyer et al. 2020), or a number density of $\sim 10^{3-4} \text{ cm}^{-3}$ (e.g. Fissel et al. 2019; Lee et al. 2021). Below the transition column density, filaments or striations are parallel to magnetic fields. Above the transition column density, dense filaments are perpendicular to magnetic fields. Pillai et al. (2020) reported a further transition in relative orientation between magnetic fields and filament, a return to parallel

* E-mail: zwchen@pmo.ac.cn

alignment at $A_V > 21$ mag (or column density $\gtrsim 2 \times 10^{22} \text{ cm}^{-2}$) in parts of the Serpens South cloud. This parallel alignment at a higher column density might be caused by gas flow towards the magnetically supercritical parts of filaments driven by gravitational collapse (Gómez et al. 2018; Pillai et al. 2020). Seifried et al. (2020) suggested that the transition from parallel to perpendicular occurs at a column density corresponding to the critical mass-to-flux ratio (M/Φ) of a cloud close to 1. Magnetically supercritical filaments, or filaments where gravity is stronger than magnetic field, are preferentially perpendicular to magnetic fields. On the other hand, magnetic fields in subcritical filaments channel the gas flow along the field lines, given that the cross field motions are resisted by Lorentz force. The bimodal orientation between filaments and magnetic field also holds for sub-Alfvénic clouds, in which the ratio of turbulent velocity dispersion δv to Alfvén speed v_A is smaller than 1. This ratio is referred as the Alfvén Mach number $M_A = \delta v/v_A$. In clouds with super-Alfvénic ($M_A > 1$) and supersonic (Mach number $\mathcal{M} > 1$) turbulence, filaments may be formed through converging flows in which magnetic fields are compressed; in this case filaments and magnetic fields are parallel and twisted (Barreto-Mota et al. 2021). Strong turbulence could be produced by violent feedback from massive stars (H II regions, stellar winds, supernova explosions). The swept-up shells by expanding H II regions look like filaments with column density higher than $\sim 10^{22} \text{ cm}^{-2}$. The magnetic fields within the shells are compressed by the supersonic shock waves, and are parallel to the filament-like shells (e.g. Krumholz et al. 2007; Arthur et al. 2011; Chen et al. 2017, 2022b). The magnetic field measurements are rather limited compared to other properties of filaments (e.g. mass, length, velocity dispersion). The poorly understood magnetic fields of filaments thus prevent a more comprehensive understanding of the dynamical states of filaments. Given the potential wealth of information stored in the magnetic field structure and strength on the formation and evolution of filaments, a more detailed investigation of the magnetic field properties in individual filaments is warranted.

Infrared dark clouds (IRDCs) are a type of dense structures, mostly appearing as filaments. IRDCs are prominent absorption features against the infrared background in the Galactic plane, and are typically located at distances of a few kpc (Carey et al. 1998; Simon et al. 2006; Peretto & Fuller 2009; Rygl et al. 2010). Massive dust condensations and cores, precursors to massive star and cluster formations, are ubiquitously found within IRDCs (Henning et al. 2010; Ragan et al. 2012). The evolution of IRDCs is expected to be governed by the combination of gravity, turbulence, and magnetic fields. However, the relative importance of these combined effects is difficult to determine. While gravity and turbulence can be explored from (sub)millimeter observations, detecting magnetic fields of IRDCs is always a challenge.

G11.11–0.12, hereafter G11, is among the first IRDCs discovered, and with the darkest shadows in the Galactic plane (Carey et al. 1998). It is located at a distance of 3.6 kpc, has a length of ~ 30 pc, a mass of $\sim 10^5 M_\odot$, and is known to host multiple star-forming sites (Pillai et al. 2006; Henning et al. 2010; Gómez et al. 2011; Shipman et al. 2014; Rosero et al. 2014; Wang et al. 2014; Pillai et al. 2019; Sanhueza et al. 2019; Li et al. 2020; Tafoya et al. 2021). The density structure of G11 can be fitted by a central massive cylinder with an extended envelope (Johnstone et al. 2003; Kainulainen et al. 2013). The spine of G11 has a linear mass density of $\sim 600 M_\odot \text{ pc}^{-1}$ that greatly exceeds the critical value of a self-gravitating, non-turbulent cylinder (Kainulainen et al. 2013). The hierarchical fragmentation in G11 indicates the dominant role of gravity that has started gravitational collapse (Kainulainen et al. 2013; Wang et al. 2014; Schneider et al. 2015; Ragan et al. 2015;

Pillai et al. 2019). The column density probability distribution function of G11 has a power-law tail in the high column density end, indicative of a gravity-dominated stage (Schneider et al. 2015; Lin et al. 2017). Signatures of gravitational collapse and longitudinal gas flow have been reported in G11 (Tremblin et al. 2014; Beuther et al. 2014; Schneider et al. 2015). It is likely that global collapse in filament scale and fragmentation in clump/core scale are simultaneously occurring in G11. Given the above observational properties, G11 is likely at a relatively late stage of filament formation. Magnetic fields, inherited from the natal ISM that G11 condensed out of, may provide additional information about the formation of G11.

Fiege et al. (2004) proposed that G11 is radially supported by predominantly poloidal magnetic fields. The magnetic fields towards G11 were first determined using $850 \mu\text{m}$ polarisation data (Pillai et al. 2015), taken with the polarimeter SCUPOL on the James Clerk Maxwell Telescope (JCMT) (Carey et al. 2000; Greaves et al. 2003). The areas observed with JCMT/SCUPOL cover a small part of the spine of G11, which is bright and compact in submillimeter wavelengths (see Figure 1 in Pillai et al. (2015)). The magnetic fields towards the densest part of G11 at sub-parsec scale are perpendicular to the long axis of the filament (Pillai et al. 2015). Generally, magnetic fields at dense core scales (≤ 0.1 pc) are either aligned with or perpendicular to the parsec scale magnetic fields (Zhang et al. 2014; Chen et al. 2020; Eswarajah et al. 2021). The link between magnetic fields in the spine of G11 (sub-parsec scale) and across the filament (parsec scale) remains unknown.

The submillimeter wavelength polarisation data from Planck mission (Planck Collaboration et al. 2011) are sensitive to large scale extended structures. However, the angular resolution of Planck 353 GHz polarisation data is worse than $\sim 5'$, which means that G11 is not well resolved by Planck data. The Planck polarisation data are the integrated contributions from dust emission along the same line of sight (LOS) to G11. Starlight polarisation, especially in the near-IR wavelengths, has the potential to reveal magnetic fields in the diffuse regions of G11. The polarisation degrees measured in multiple wavelengths were found to follow the Serkowski relation (Serkowski et al. 1975; Whittet et al. 1992), confirming the interstellar origin for starlight polarisation. When the background starlight polarisation is carefully analysed, the starlight polarisation due to dust extinction in G11 carries the information of dust alignment. In diffuse ISM, elongated dust grains with short axes parallel to magnetic fields can be explained by the radiative torque mechanism (Lazarian & Hoang 2007; Andersson et al. 2015). The linear polarisation of starlight due to dust extinction is widely used to probe for the on-sky component of magnetic fields (hereafter B_{sky}), which is parallel to starlight polarisation angle. In this paper, we present the large scale magnetic fields of G11, derived from near-IR starlight polarisation of background stars. The study of the large scale magnetic fields is essential to explore the effects of magnetic field in the formation and evolution of G11.

2 DATA ACQUISITION

2.1 IRSF/SIRPOL Observations

The data were taken with SIRPOL on the 1.4 m InfraRed Survey Facility (IRSF) telescope at the South African Astronomical Observatory, Sutherland, South Africa. SIRPOL is a single-beam polarimeter capable of simultaneous imaging polarisation observations in the near-IR JHK_s bands with an $\sim 8' \times 8'$ field of view

(FOV)(Nagayama et al. 2003; Kandori et al. 2006). The observations were made during the night of 2018 July 21. To cover the entire extent of G11, we designed a mosaic of three frame positions around the location of G11, as shown in Figure 1. In each frame position, three sets of observations were taken. In each set, the telescope was dithered at 10 positions, each with 30 s exposure time at 4 wave-plate angles in a sequence of 0° , 45° , 22.5° , and 67.5° . The total integration time was 1200 s per wave-plate angle in each of the three frame positions. The total observation time in each of the three frame positions was 83 min, taking observation overheads into account. The total observation time for all the three frame positions was 4.1 hr. The airmass during the observations was in the range of 1.03 – 1.60. Observations with lower airmass generally have narrower full width at half maximum (FWHM). The average FWHM for the point sources in all the three frame positions were determined by ranging from around 3 to 4 pixels, or $\sim 1''.5$ – $1''.8$ ($0''.45$ per pixel).

In the same night of the IRSF observations, a field from the Galactic Plane Infrared polarisation Survey (GPIPS) (Clemens et al. 2012) was observed with SIRPOL just before the observations for G11. The original field GP0006 from GPIPS is centered on $R.A.(J2000) = 18^h26^m11^s.2$, $Decl.(J2000) = -13^\circ19'57''$, and has a $10' \times 10'$ FOV. The SIRPOL images for the GP0006 field are centered on the inner $\sim 8' \times 8'$ region, slightly smaller than the original FOV of the GP0006 field.

The data reduction and aperture photometry for the JHK_s polarimetric observations of G11 and the GP0006 field are referred to in Chen et al. (2022b). Following the procedures used in determining polarisation measurements in Chen et al. (2022b), we obtained the JHK_s polarisation measurements of sources towards G11 and the GP0006 field. The polarisation measurements have a positive bias because the polarisation degree derived from $\sqrt{Q^2 + U^2}$ is always positive, even though the normalized Stokes parameters Q and U can be either positive or negative. Following the methods of correcting this positive bias (Wardle & Kronberg 1974; Hull & Plambeck 2015), the bias-corrected polarisation is $P = \sqrt{Q^2 + U^2 - \delta P^2}$. In the following texts, the bias-corrected polarisation is labeled as P , unless otherwise noted. The polarisation position angle θ_{PA} is measured counterclockwise from the north to the east using equatorial coordinates. The 1σ uncertainty of θ_{PA} depends on the polarisation signal-to-noise ratio $\frac{P}{\delta P}$. For simplicity, the 1σ uncertainty of θ_{PA} is obtained from the standard formula $\delta\theta_{PA} = 28.6 \delta P/P$. For sources with $\frac{P}{\delta P} \geq 6$, the 1σ uncertainty of θ_{PA} obtained as outlined above is reliable (Naghizadeh-Khouei & Clarke 1993). For lower SNR ($2 \leq \frac{P}{\delta P} < 6$), the 1σ uncertainty of θ_{PA} is underestimated, with smaller deviation for higher $\frac{P}{\delta P}$. More than 85% of the observed sources towards G11 in all the JHK_s bands meet the criterion $\frac{P}{\delta P} \geq 3$, which means that majority of the sources considered in this work have 1σ uncertainty of θ_{PA} of less than 10° .

The H -band starlight polarisation obtained with SIRPOL towards the GP0006 field of GPIPS are compared to the GPIPS catalog (Clemens et al. 2012, 2020). We found 13 polarised stellar sources common in both our SIRPOL observations and the GPIPS catalog. These stellar sources satisfy $P_H/\delta P_H \geq 6$ and $2MASS J-H \geq 0.9$, and have P_H in the range from 1% to 9% and θ_{PA} in the range from 10° to 180° . For the 13 stellar sources, the mean difference in P_H relative to the GPIPS value is -6.2% with a standard deviation of 16.3%; the mean difference in θ_{PA} relative to the GPIPS value is 7.8° with a standard deviation of 7.6° . The SIRPOL observations of the GP0006 field show tight consistency with the GPIPS catalog. For the simultaneous observations in the JHK_s bands with the IRSF telescope, the JK_s -band starlight polarisation are aligned in polar-

isation orientations with the H -band polarisation. For tracing the on-sky magnetic field component, B_{sky} , only the polarisation orientations are utilized. The starlight polarisation in the JHK_s bands of the H II regions M17 and RCW 120 show consistency in polarisation orientations in all three bands (Chen et al. 2012, 2022b), though a dependence of polarisation degree with the wavelength was observed (Chen et al. 2012).

2.2 VVVX photometry

We used the near-IR photometry from the extension of the Vista Variables in the Vía Láctea (hereafter VVVX) survey (Minniti et al. 2010). G11 was covered in tile e0954 as part of the VVVX Data Release 1. The JHK_s images and catalogs of the e0954 tile were retrieved from the European Southern Observatory (ESO) Science Archive Facility¹. The VVVX JHK_s catalogs include magnitudes from a series of aperture diameters, ranging from $1''$ to $24''$ (aperture 1 to aperture 13). The aperture 3 corresponds to an aperture diameter of $2''$. We utilized the aperture 3 measurements of the VVVX photometric catalog. The calibrated JHK_s magnitudes can be derived from the aperture 3 fluxes using the following equation:

$$CalMag = MAGZPT - 2.5 \log Flux - APCORN, \quad (1)$$

where the zero point calibration $MAGZPT$ and aperture correction term $APCORN$ of aperture 3 are integrated in the same VVVX catalog².

2.3 CO Molecular Line Data of G11

The CO and CO isotopologues $J=1-0$ data of G11 were obtained from the Milky Way Imaging Scroll Painting (MWISP) project, an unbiased Galactic plane CO survey in the northern sky using the 13.7 m millimeter-wavelength telescope at Delingha, China (see Su et al. 2019, for more details). A linear baseline was subtracted from the ^{12}CO , ^{13}CO , and C^{18}O $J=1-0$ spectra. After the calibration of the main beam efficiency of $\sim 50\%$, the reduced position-velocity (PPV) cubes with a $30'' \times 30''$ grid are on the intensity scale of main beam temperature, T_{MB} . The measured root-mean-square (rms) noise is ~ 0.5 K for ^{12}CO $J=1-0$ spectra and ~ 0.3 K for $^{13}\text{CO}/\text{C}^{18}\text{O}$ $J=1-0$ spectra at a channel width of 61 kHz (≈ 0.16 – 0.17 kms^{-1}). The angular resolutions of the CO PPV cubes are close to $50''$.

Similar to the velocity range of $26 - 35$ km s^{-1} of ^{12}CO $J=3-2$ emission presented in Schneider et al. (2015), we utilized a wider velocity range of $25 - 37$ km s^{-1} , based on the ^{12}CO and ^{13}CO $J=1-0$ emission. With this velocity range, we derived the moment 0 (integrated intensity), moment 1 (velocity), and moment 2 (line width) maps of the ^{12}CO , ^{13}CO and C^{18}O $J=1-0$ emissions from the MWISP CO PPV cubes. The excitation temperature, T_{ex} , of the CO molecular gas was derived from the ^{12}CO $J=1-0$ spectra, following Equation 9 in Chen et al. (2022b). The pixel-wise T_{ex} map across G11 is uniform with a median of 12 K, and a standard deviation of 1 K. Assuming that the molecular gas is in the state of local thermal equilibrium (LTE), the ^{13}CO and C^{18}O gas share the same T_{ex} of the ^{12}CO gas. In the state of LTE, we derived the column densities of ^{13}CO and C^{18}O gas ($N(^{13}\text{CO})$ and $N(\text{C}^{18}\text{O})$) according to Equation 10 in Chen et al. (2022b). Following Equation 11 in Chen et al.

¹ The VVVX datasets are available at <https://doi.eso.org/10.18727/archive/68>

² See <https://www.eso.org/rm/api/v1/public/releaseDescriptions/187>

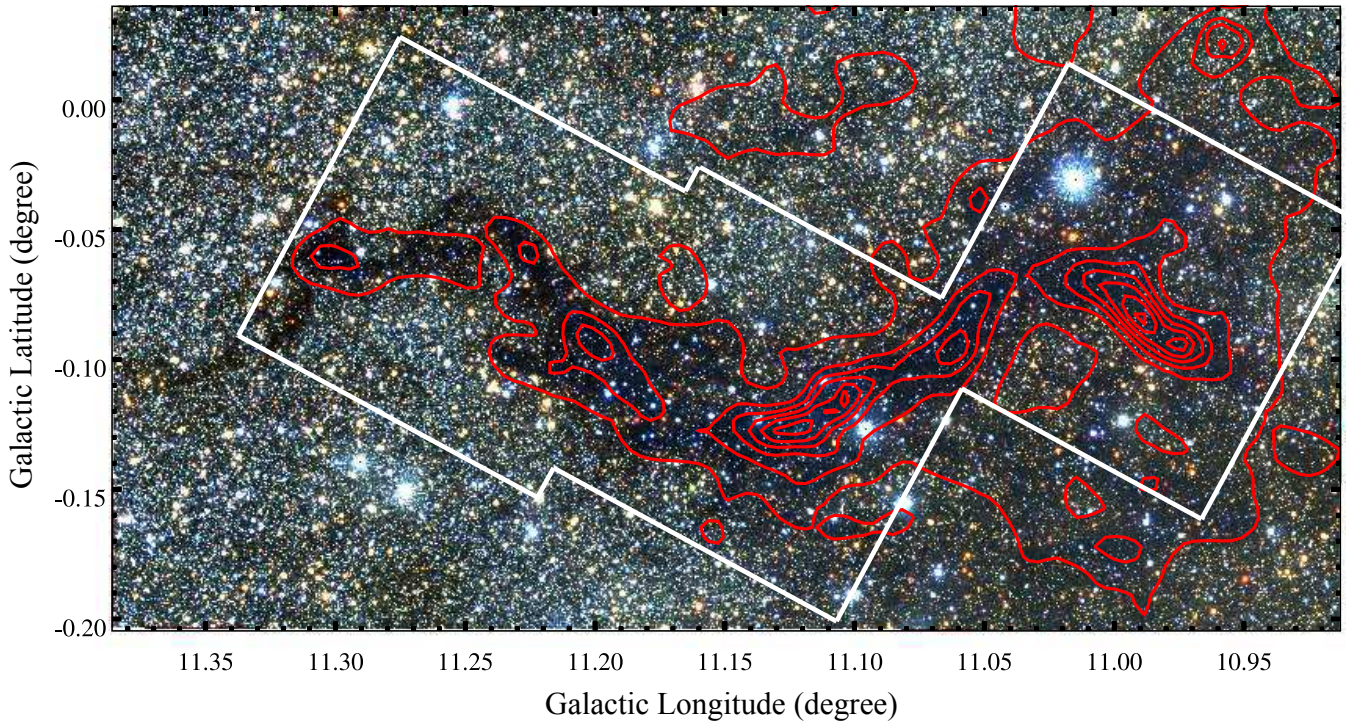


Figure 1. Three-colour composite image of G11, made from the VVVX J (blue), H (green), and K_s (red) images, overlaid with the red contours of $N(\text{H}_2)_{\text{dust}}$ from $2 \times 10^{22} \text{ cm}^{-2}$ to $8 \times 10^{22} \text{ cm}^{-2}$ in steps of 10^{22} cm^{-2} . The coverage of the IRSF observations is marked by the inserted grid shape made from three different pointings of IRSF, within the white lines and as discussed in Section 2.1.

(2022b), the optical depth τ_{13} of the ^{13}CO emission reaches a maximum value ≈ 1 towards the densest regions of G11. In the remaining parts of lower density in G11, τ_{13} varies mostly between 0.3 and 0.7. The $N(^{13}\text{CO})$ was then multiplied by the optical depth correction factor, $\frac{\tau_{13}}{1 - \exp(-\tau_{13})}$. We simply assumed that the optical depth of $\text{C}^{18}\text{O } J=1-0$ emission is $\ll 1$. Thus the optical depth correction factor for the C^{18}O emission is ≈ 1 . Assuming the H_2 to ^{13}CO and C^{18}O abundance ratios as 5×10^5 and 3.5×10^6 , respectively (Chen et al. 2022b, and references therein), we derived molecular hydrogen column density $N(\text{H}_2)$ from $N(^{13}\text{CO})$ and $N(\text{C}^{18}\text{O})$ respectively. The moment 2 map of the ^{13}CO emission evaluates the velocity dispersion δv across G11, which has a narrow distribution with a median of 1.9 km s^{-1} and a standard deviation of 0.2 km s^{-1} . Meanwhile the sound speed c_s is around 0.2 km s^{-1} across G11, corresponding to a rather uniform $T_{\text{ex}} \sim 12 \text{ K}$ derived from the ^{12}CO line emission. The molecular gas is supersonic, characterized by the Mach number ($\mathcal{M} = \delta v / c_s$) > 6 across G11. The column density, velocity field and velocity dispersion of molecular gas derived from CO PPV cubes and magnetic fields traced by near-IR starlight polarisation are the fundamental parameters characterizing the dynamical state of G11.

2.4 Column Density Map from Herschel

The $N(\text{H}_2)_{\text{dust}}$ map of G11 was constructed from the modified blackbody fit to the Herschel maps at 160, 250, 350 and $500 \mu\text{m}$ (see Schneider et al. 2015, for further details). The $N(\text{H}_2)_{\text{dust}}$ map of G11 was smoothed to an angular resolution of $\sim 36''$, slightly better than the angular resolution of the MWISP CO data.

3 RESULTS

Figure 1 shows a three-colour composite image of G11 from the VVVX observations. The combined IRSF observations cover the entire G11 filamentary dark cloud and sufficient areas around the filament, an indication that the near-IR polarisation observations span the entire dense filament and surrounding fields of lower gas emission (see also Figure 3). The red contours of $N(\text{H}_2)_{\text{dust}}$, superimposed on the composite image in Figure 1, also cover the entire filamentary region.

The near-IR polarisation observations from the IRSF telescope can potentially be used to trace magnetic fields in the surrounding fields of lower density. However, the dense filament in G11.11-0.12 has $N(\text{H}_2)_{\text{dust}}$ well above $4 \times 10^{22} \text{ cm}^{-2}$, which is beyond the starlight polarisation detection limit of the IRSF (a 1.4 m class telescope) in the near-IR wavelengths. Near-IR polarisation observations by a larger telescope may have sufficient sensitivity to detect the faint polarised starlight of background stars lying behind the spine of G11.

3.1 Analysis of Reddened Background Stars

The IRSF observations are not deep enough to detect sufficient background stars, especially in the J band. Similar to the approach used in Chen et al. (2017, 2022b), we combine the JHK_s starlight polarisation ($P_\lambda \geq 2\delta P_\lambda$) with the VVVX photometry. Applying a search radius of $1''$, there are 637 sources in the J band, 749 sources in the H band, and 624 sources in the K_s band, that have starlight polarisation $P_\lambda \geq 2\delta P_\lambda$ and JHK_s photometry from VVVX. The VVVX sources with starlight polarisation have a mean FWHM of $0''.9$, a value not too much smaller than the mean FWHM ($\sim 1''.5 - 1''.8$) of the IRSF observations. Although the IRSF observations have larger FWHM than the mean FWHM of VVVX sources, the cross-match

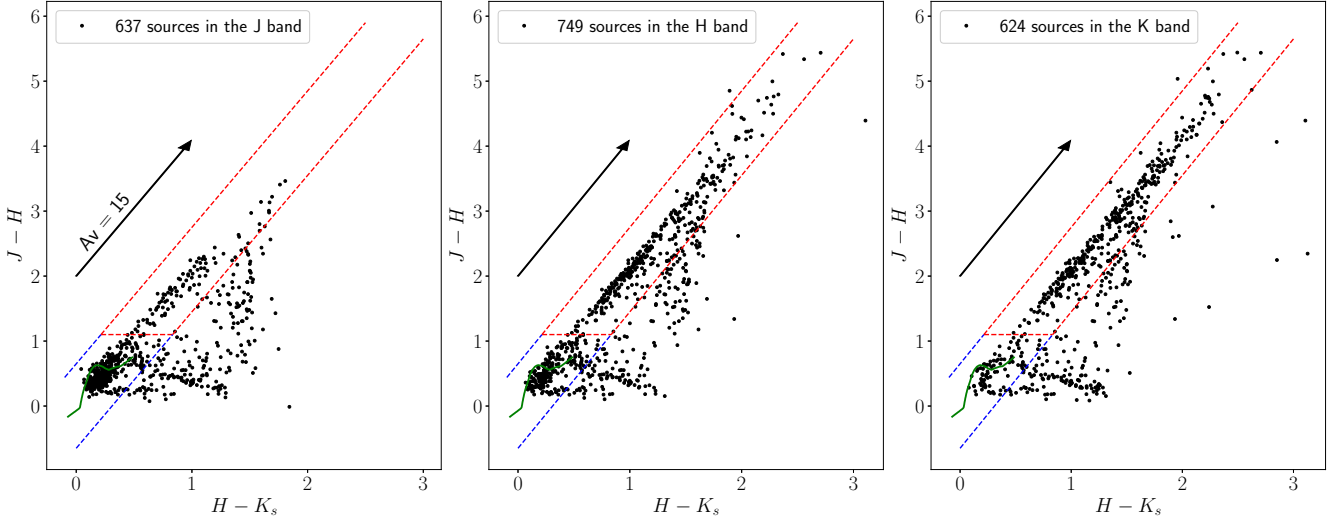


Figure 2. $J - H$ vs. $H - K_s$ colour-colour diagrams of the sources in the JHK_s bands from left to right respectively. The main-sequence intrinsic colours (highlighted in green) are adopted from Pecaut & Mamajek (2013). The background and foreground stars are lying within the areas enclosed by the red and blue dashed lines respectively. A reddening vector of length $A_V = 15$ mag is displayed as the arrow.

Table 1. The foreground-corrected polarisation in the K_s band and VVVX JHK_s photometry of the 364 background stars towards G11.

ID	R.A. (J2000)	Decl. (J2000)	P_K (%)	δP_K (%)	θ_{PA} ($^\circ$)	$\delta\theta_{PA}$ ($^\circ$)	J (mag)	Jerr (mag)	H (mag)	Herr (mag)	K (mag)	Kerr (mag)
1	272.51927	-19.52159	2.1	0.1	27.0	1.0	14.900	0.004	12.004	0.001	10.395	0.001
2	272.48228	-19.51889	1.7	0.1	85.4	1.9	14.393	0.003	12.118	0.001	10.927	0.002
3	272.54558	-19.51703	4.3	0.1	43.8	0.8	17.315	0.029	13.329	0.003	11.383	0.002
4	272.46133	-19.51687	4.4	0.4	19.3	2.8	18.563	0.088	14.320	0.008	12.303	0.005
5	272.50304	-19.51593	1.9	0.8	60.0	10.3	16.187	0.011	13.773	0.005	12.599	0.006
6	272.55243	-19.51442	3.3	0.2	32.9	1.9	17.374	0.030	13.673	0.004	11.878	0.003
7	272.47824	-19.51363	1.0	0.2	61.2	4.1	15.065	0.005	12.595	0.002	11.448	0.002
8	272.49046	-19.51009	1.1	0.4	113.6	12.2	16.133	0.011	13.597	0.004	12.390	0.005
9	272.57179	-19.50984	3.5	0.1	18.8	0.5	15.717	0.008	12.062	0.001	10.338	0.001
10	272.54242	-19.50795	2.6	0.2	41.7	1.9	14.667	0.004	12.544	0.002	11.548	0.002

Only a portion of this table is shown here. The full version is available online (Chen et al. 2022a).

between the starlight polarisation and VVVX catalog is mostly one-to-one. In the K_s band sample of 624 sources with polarisation and VVVX photometry, as an example, only one source has another fainter source from the VVVX catalog within a $2''$ radius. The fractions of blended sources are believed to be very low for the starlight polarisation samples in the JHK_s bands.

We applied the classical $J-H$ versus $H-K_s$ colour-colour diagram to classify background stars that mostly show large $J-H$ and $H-K_s$ colours. Figure 2 shows the colour-colour diagram for the starlight polarisation with the VVVX photometry in the JHK_s bands. Two populations exist in the colour-colour diagrams, stars with low $H-K_s$ and $J-H$ colours, and those reddened to higher colours along the extinction line. Similar to the criteria in Chen et al. (2022b), the criteria for background stars with respect to G11 are

$$J - H \leq 2.1 \times (H - K_s) + 0.65 \quad (2)$$

$$J - H \geq 2.1 \times (H - K_s) - 0.65 \quad (3)$$

$$J - H \geq 1.1, \quad (4)$$

and are displayed as the red dashed lines in Figure 2. Stars enclosed by the blue dashed lines are classified as the foreground stars with respect to G11. The $J-H \geq 1.1$ threshold for classifying background

stars is a compromise value neither too high nor too low, and is chosen mainly based on our experience and the source distributions in the colour-colour diagram in Figure 2. Because the distance to G11 is 3.6 kpc, 2 times that to the RCW 120 region (Chen et al. 2022b), the interstellar extinction caused by diffuse ISM towards G11 is likely higher than that for RCW 120. The higher interstellar extinction by diffuse ISM is represented by the $J - H \geq 1.1$ criterion for G11, higher than $J - H \geq 0.9$ applied for RCW 120 (Chen et al. 2022b). The numbers of foreground stars are 341, 232, 86 in the J , H and K_s bands, respectively. In contrast, the numbers of background stars are 97, 334, and 364 in the J , H and K_s bands, respectively. In the short wavelengths, starlight polarisation is dominated by foreground stars. The numbers of background stars with polarisation in more than two bands are largely reduced. For example, 60 background stars meet the criterion, $P_\lambda \geq 2\delta P_\lambda$, in all the three bands. The number of background stars with polarisation of $P_\lambda \geq 2\delta P_\lambda$ in both H and K_s bands is 237, a value much lower than that in the H or K_s band.

The Gaia mission provides accurate stellar parallaxes up to several kilo parsecs (Gaia Collaboration et al. 2016, 2021), depending on the level of interstellar extinction along the LOS. From the star distance catalog (Bailer-Jones et al. 2021), we retrieved distance es-

estimates of JHK_S starlight polarisation by using a match radius of $1''$. We considered the sources with narrow range of distance estimates, defined by $(B_{r_{geo}} - b_{r_{geo}})/r_{geo} < 0.2$, where $B_{r_{geo}}, b_{r_{geo}}, r_{geo}$ are the 84th percentile, the 16th percentile, and the median value of the geometric distance posterior (Bailer-Jones et al. 2021).

The fraction of foreground stars with available distance estimates from Gaia is between $1/3$ to $1/2$ of all foreground stars detected in the JHK_S bands. We found no background stars observed in the JHK_S bands with accurate distance estimates, indicating that the observed background stars are most likely too far and/or highly reddened (e.g. Chen et al. 2013). A robust classification of background stars relative to G11 relies on distance. Nevertheless, the smaller extinction in the K_S band would, therefore, lead to more stars detected behind G11. In contrast, fewer stars behind G11 are detectable in the J and H bands, which have relatively larger extinction. Background stars observed in the K_S band are generally more distant and more likely to be lying behind G11. In fact, background stars observed in the K_S band (364 stars) are comparatively more than those detected in the J and H bands (97 and 334 stars, respectively). The starlight polarisation of background stars in the K_S band is, therefore, more likely to be resulting from the dust grains within G11. In this paper, we analyse the K_S -band starlight polarisation of 364 background stars.

3.2 Foreground polarisation

The interstellar polarisation arising from foreground dust in front of G11.11-0.12 is not negligible and therefore should not be ignored. For the 39 foreground stars with distances < 3 kpc, no trend is found for the K_S -band polarisation degree with respect to distance. The weighted K_S -band mean polarisation degree of these 39 foreground stars is $1.3 \pm 0.1\%$. Those contributions should be removed from the starlight polarisation of background stars prior to the analyses of magnetic fields. This correction of foreground polarisation has been widely applied when the foreground polarisation is significant and ordered (e.g. Clemens et al. 2013; Eswaraiah et al. 2019; Devaraj et al. 2021). The foreground polarisation can be neglected in cases where it is small and random (e.g. Chen et al. 2017).

Foreground polarisation towards G11 in the K_S band was computed from the starlight polarisation of 86 foreground stars. The spatial distributions of foreground polarisation are split into grids with a spacing of $5'$. The weighted Stokes mean values of the foreground contribution in a grid is computed from the foreground polarisation within the same grid. Every background star is assigned to a nearest grid with computed foreground polarisation. The corrected Stokes values of background stars are $Q_{\text{cor}} = Q_{\text{bg}} - Q_{\text{fg}}$ and $U_{\text{cor}} = U_{\text{bg}} - U_{\text{fg}}$. The foreground-corrected polarisation degree (P_K), and position angle (θ_{PA}) are calculated using Equations (6) and (7) in Chen et al. (2022b). The foreground-corrected starlight polarisation of the 364 background stars in the K_S band are used to trace the local B_{sky} of G11. Table 1 lists the foreground-corrected polarisation in the K_S band and VVXX photometry in JHK_S -bands of the 364 background stars. The values of θ_{PA} in Table 1 are read counterclockwise from the equatorial north, following the IAU definition.

3.3 The Local B_{sky} in G11

Figure 3 shows the orientation of the foreground-corrected K_S -band polarisation (green segments) of the background stars superimposed on the $N(\text{H}_2)$ map derived from ^{13}CO emission. The K_S -band polarisation segments were rotated by a specific angle to match the Galactic

coordinate frame of Figures 3, 4, 7 and 8. Besides the polarization orientation of individual background stars shown in Figure 3, we also split the starlight polarisation into each cell of $2' \times 2'$ size. Table 2 lists the properties of each cell, including positions of the cell center, weighted mean polarisation (degrees and orientations), average gas velocity, the absolute difference between polarisation orientation and the filament orientation, and the number of polarisation vectors. We keep only the cells with at least three polarisation vectors. The $2' \times 2'$ cell is moderate, so that each effective cell contains eight starlight polarisation in average. In Figure 4 the mean orientation of starlight polarisation in each cell was displayed as green segments, overlaid on the map of polarisation angle dispersion in each cell.

The spine of G11, better traced by the $N(\text{H}_2)_{\text{dust}}$ contours, clearly shows a positive gradient of column density, from left to right. The spine of G11 is, in fact, twisted along the Galactic plane, and can be divided into four regions with different orientations relative to the Galactic plane. The spine orientations of the four regions, read counterclockwise from the equatorial north, were determined by the visual inspection of the highest $N(\text{H}_2)_{\text{dust}}$ isocontours in each region.

Region A: $11^\circ 24 < l < 11^\circ 34$; the spine here has the lowest $N(\text{H}_2)_{\text{dust}}$ of $\sim 2 \times 10^{22} \text{ cm}^{-2}$, with a peak value of $3.6 \times 10^{22} \text{ cm}^{-2}$. The envelope of region A has even lower column density, $\sim 0.5 \times 10^{22} \text{ cm}^{-2}$, derived from the $^{13}\text{CO } J=1-0$ emission.

Region B: $11^\circ 15 < l < 11^\circ 24$; the spine of region B has a peak $N(\text{H}_2)_{\text{dust}}$ of $4.7 \times 10^{22} \text{ cm}^{-2}$, higher than that of region A. The envelope here has column density $\sim 0.8 \times 10^{22} \text{ cm}^{-2}$.

Region C: $11^\circ 04 < l < 11^\circ 15$; the spine here contains the densest and most massive dust condensation, P1 (Johnstone et al. 2003), in which massive star formation is evident (e.g. Pillai et al. 2006; Shipman et al. 2014; Rosero et al. 2014). The peak $N(\text{H}_2)_{\text{dust}}$ reaches $7.7 \times 10^{22} \text{ cm}^{-2}$ towards the dust condensation P1. The magnetic fields in the spine of this region are perpendicular to the filament itself (Pillai et al. 2015), as indicated by the white segment in Figure 3.

Region D: $10^\circ 93 < l < 11^\circ 04$; the spine of region D has a peak $N(\text{H}_2)_{\text{dust}}$ of $8.3 \times 10^{22} \text{ cm}^{-2}$ towards its densest part, and is almost as dense as that of region C. It contains the massive dust condensation P6 (Johnstone et al. 2003; Wang et al. 2014) and the $70 \mu\text{m}$ dark clump G10.99–0.08 (Pillai et al. 2019; Sanhueza et al. 2019), in which star formation is still on-going.

The orientations of the foreground-corrected K_S -band polarisation in the four regions of G11 are displayed in the top rows of Figure 5. The orientations of mean starlight polarisation in cells in the four regions are shown in the bottom rows. In regions A, B and C, the overall orientations of starlight polarisation are in the range $130 - 150^\circ$. The starlight polarisation in region A shows a narrow distribution, with a peak at 132° . The orientations of starlight polarisation in region B are similar to those in region A, but show a larger scatter. In areas of region B adjacent to region A, the orientations of starlight polarisation are parallel to those in region A. The orientations of starlight polarisation in region C have a peak at 147° , roughly parallel to those in regions A and B. The orientations of starlight polarisation in region D peak at 32° , roughly perpendicular to those in regions A, B and C.

The cutout 353 GHz Stokes I, Q, U maps with pixel scale of $1.7'$ for G11 were retrieved from the Planck Legacy Archive³. The Planck I, Q, U maps were smoothed to $5.1'$ resolution using a Gaussian kernel with FWHM = 3 pixels. The 353 GHz dust polarisation degree and polarisation orientation in the IAU definition were com-

³ <http://http://pla.esac.esa.int/pla>

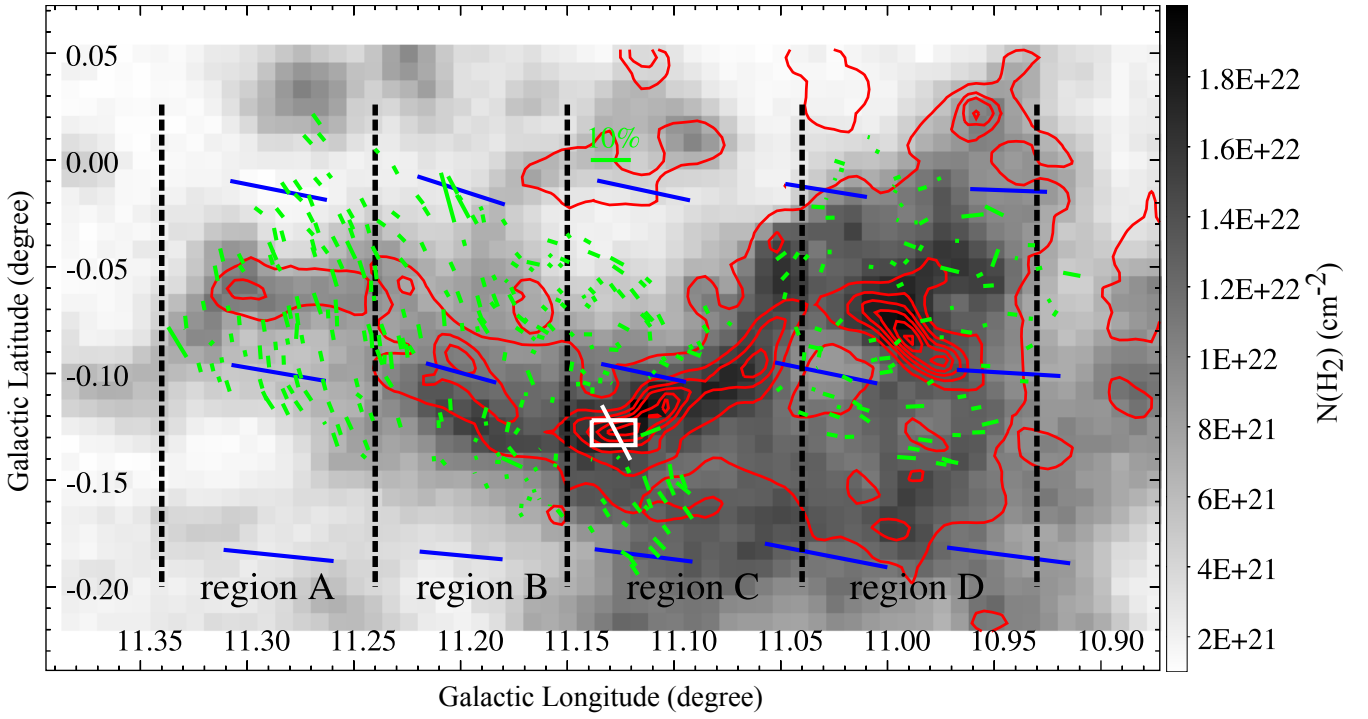


Figure 3. Molecular hydrogen column density derived from $^{13}\text{CO } J=1-0$ emission in the velocity range $25\text{--}37 \text{ km s}^{-1}$, overlaid with the red contours of $N(\text{H}_2)_{\text{dust}}$ from $2 \times 10^{22} \text{ cm}^{-2}$ to $8 \times 10^{22} \text{ cm}^{-2}$ in steps of 10^{22} cm^{-2} . The foreground-corrected K_s -band starlight polarisation is displayed as the green segments with lengths in proportion to polarisation degree. The blue segments with a grid spacing of $5' \times 1'$ represent the magnetic field orientations, rotated 90° from the Planck 353 GHz dust polarisation angle. The mean degree of 353 GHz dust polarisation is 1.6%. The length of the blue segment is in an arbitrary scale. The white rectangle outlines the region for which JCMT $850 \mu\text{m}$ dust polarisation was analyzed (Pillai et al. 2015). The mean orientation of $850 \mu\text{m}$ dust polarisation is displayed as the white segment.

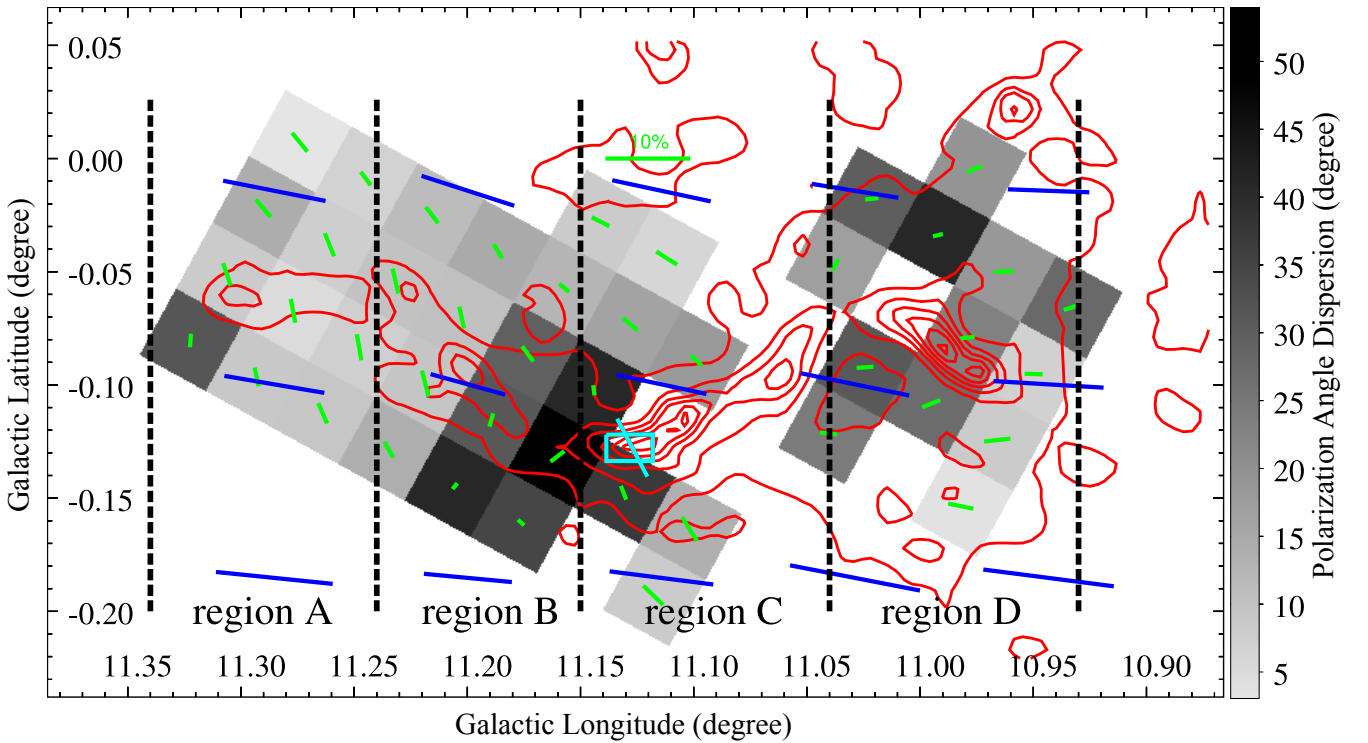


Figure 4. Polarisation angle dispersion map with a grid spacing of $2' \times 2'$. The mean polarisation in each cell are displayed as the green segments with lengths in proportion to the mean polarisation degree. The blue segments, red contours, cyan rectangle and segment are the same as in Figure 3.

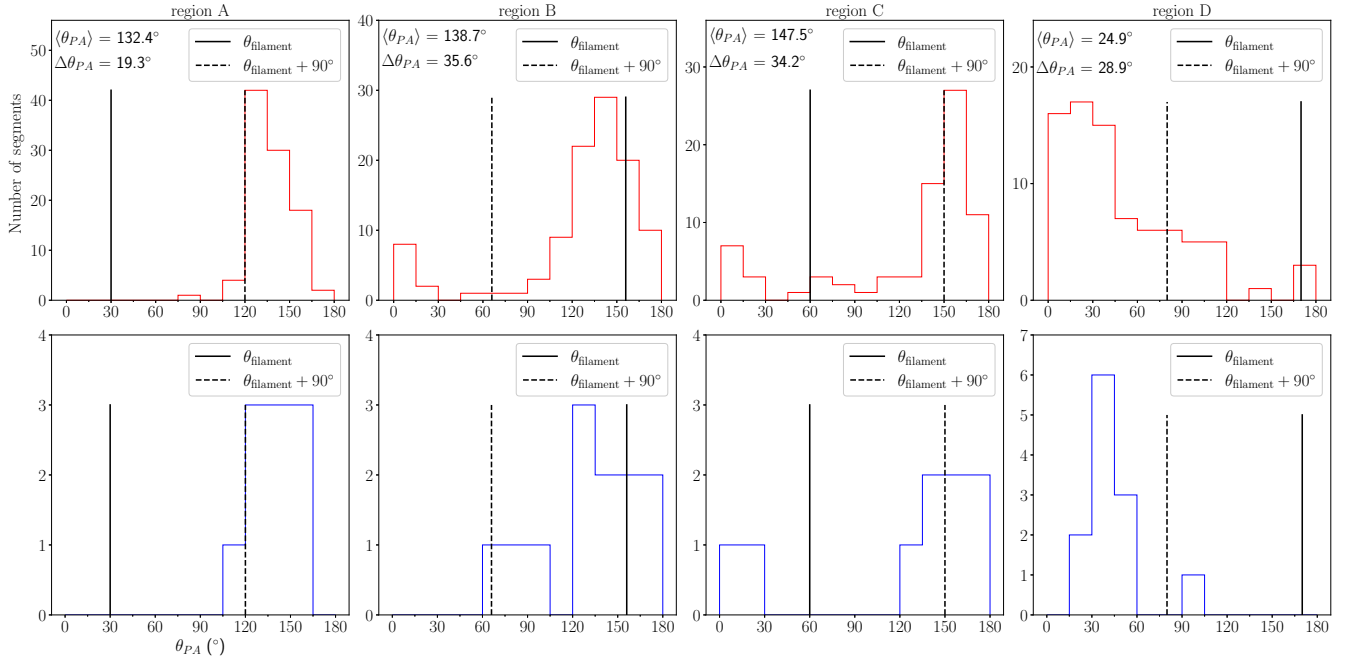


Figure 5. Top: Histograms of the orientations of the foreground-corrected K_s -band polarisation in the four regions of G11. The orientations of the spines in the four regions are marked by the vertical black solid lines. The orthogonal orientations of the spines are marked by the vertical dashed lines. Bottom: Same as top, but for the mean orientation in each cell.

puted from the Stokes I, Q, U maps, following Equations 1 and 2 in Planck Collaboration et al. (2015). The magnetic field orientations on the plane of the sky are displayed as the blue segments in Figures 3 and 4. The magnetic field orientations, rotated 90° from the Planck dust polarisation angle, are compared with the field orientations traced by the foreground-corrected starlight polarisation angles. The average offsets in magnetic field orientations traced by the two methods are 68° , 57° , 50° , and 4° in regions A, B, C, and D respectively, an indication that magnetic fields traced by starlight polarisation are very different from the field orientations traced by dust polarisation in most parts of the G11 filament. G11 is lying within the Galactic plane, along which direction the Planck dust polarisation data record all the polarised dust emission along the same LOS. The LOS contamination might be much less severe for the filaments at high Galactic latitude. Soler et al. (2016) compared the orientation of magnetic field projected on the plane of the sky inferred from the Planck 353 GHz dust polarisation and optical/infrared starlight polarisation for four nearby molecular clouds at high Galactic latitude. The consistency between field orientation sampled in the dust polarised emission and dust extinction suggests considerable agreement between the magnetic field orientation on the plane of the sky estimated with both techniques at comparable scales (Soler et al. 2016). Because of the severe LOS contamination, the Planck dust polarised emission towards G11 are inadequate in tracing the local magnetic field of this filament.

Figure 5 compares the polarisation orientations with the spine orientations in the four regions. In both regions A and C, the orientations of starlight polarisation are perpendicular to their spines. The mean starlight polarisation in the cells within region B show a bimodal distributions. In areas of region B adjacent to region A, the starlight polarisation is roughly parallel to the spine of region B. In the rest parts of region B, the grid-averaged starlight polarisation tends to be perpendicular to the spine of region B, but with higher dispersion, as shown by Figure 4. The projection effects of the magnetic field and

filaments can produce small relative orientation angles between the filament and the magnetic field projected onto the plane of the sky, even though the magnetic field is orthogonal to the filament in a 3D space (Doi et al. 2020). The observed parallel orientation between the starlight polarisation and the spine in region B is likely to be due to the projection effects. The orientations of starlight polarisation in region D are almost perpendicular to those in regions A, B and C. However, the grid-averaged starlight polarisation in region D is close to being perpendicular to the spine of region D. The orientations of the foreground-corrected K_s -band polarisation in the four regions are generally perpendicular to the spines in each region, despite the fact that the spines in each region have different orientations.

The $N(\text{H}_2)_{\text{dust}}$ in the spine of region C is $\geq 4 \times 10^{22} \text{ cm}^{-2}$. Few starlight polarisation was detected towards the spine of region C. Starlight polarisation traces better the B_{sky} in the surrounding envelope of region C. The B_{sky} traced by starlight polarisation in the envelope is consistent with the magnetic fields on the spine of region C obtained from dust polarisation (Pillai et al. 2015). The consistency of B_{sky} in the envelope of parsec scales, and the dense core of sub-parsec scales, indicates that magnetic fields are perpendicular to the spine of region C. Combining the near-IR starlight polarisation in this work and the dust polarisation in Pillai et al. (2015), the magnetic fields are found to be always perpendicular to G11 across the parsec-scale envelope surrounding the filament to the dense spine in which star formation is on-going.

3.4 Strength of B_{sky}

The variable extinction across G11 leads to the non-uniform spatial distribution of starlight polarisation. The number of starlight polarisation towards the low-density envelope of G11 is much higher than that towards the high-density spine. Therefore, the magnetic field strength is more representative of the envelope rather than the dense spine of G11. Pillai et al. (2015) estimated a total magnetic strength

Table 2. Mean starlight polarisation and mean gas velocity dispersion in each cell of $2' \times 2'$ size.

Region	R.A. (J2000)	Decl. (J2000)	$\langle P_K \rangle$ (%)	$\langle \theta_{PA} \rangle$ ($^\circ$)	δv (km s^{-1})	$ \langle \theta_{PA} \rangle - \theta_{\text{filament}} $ ($^\circ$)	N_{pol}
A	272.6600	-19.1720	2.9	135.5	1.5	74.5	6
A	272.6600	-19.2053	3.0	128.1	1.7	81.9	10
A	272.6600	-19.2387	3.2	127.1	1.7	82.9	11
A	272.6247	-19.2053	3.0	139.2	1.4	70.8	15
A	272.6953	-19.1720	1.7	112.6	1.6	82.6	11
A	272.6953	-19.2053	2.3	129.6	1.8	80.4	12
A	272.6248	-19.1720	2.7	157.8	2.3	52.2	9
A	272.6953	-19.2387	2.7	140.5	1.9	69.5	15
A	272.5894	-19.2053	2.0	154.3	2.2	55.7	4
A	272.5895	-19.1720	2.9	156.9	2.2	53.1	4
B	272.6247	-19.2387	3.1	130.3	1.6	25.7	7
B	272.6600	-19.2720	3.3	131.2	1.8	24.8	7
B	272.6600	-19.3053	1.7	101.8	1.8	54.2	8
B	272.6600	-19.3387	2.1	67.5	1.7	88.5	8
B	272.6247	-19.2720	2.7	129.3	1.8	26.7	11
B	272.6247	-19.3053	2.2	153.9	1.8	2.1	10
B	272.6953	-19.2720	2.2	147.2	1.8	8.8	4
B	272.6953	-19.3053	0.9	81.9	2.0	74.1	5
B	272.6953	-19.3387	1.0	165.0	2.1	9.0	10
B	272.5894	-19.3053	1.5	168.0	2.2	12.0	14
B	272.5894	-19.2720	2.0	148.8	1.9	7.2	11
B	272.5894	-19.2387	2.4	155.1	2.0	0.9	9
C	272.6600	-19.3720	1.8	138.4	1.8	78.4	5
C	272.6247	-19.3387	1.2	124.1	1.9	64.1	11
C	272.6600	-19.4053	3.3	149.3	1.9	89.3	13
C	272.5893	-19.3720	1.8	164.2	2.1	75.8	11
C	272.5894	-19.3387	2.3	168.3	2.8	71.7	14
C	272.6953	-19.4053	3.3	163.9	2.0	76.1	4
C	272.5893	-19.4387	2.1	24.0	1.9	36.0	7
C	272.5540	-19.3387	2.9	176.1	2.5	63.9	4
C	272.5541	-19.3053	2.3	1.9	2.5	58.1	3
D	272.5539	-19.4387	2.0	34.5	2.0	44.5	9
D	272.5539	-19.4720	2.4	52.5	2.0	62.5	7
D	272.5186	-19.4720	1.7	37.1	2.1	47.1	5
D	272.5185	-19.5053	2.2	28.9	2.5	38.9	4
D	272.4832	-19.4720	2.4	33.2	2.5	43.2	5
D	272.4832	-19.4387	1.2	44.1	2.0	54.1	10
D	272.5186	-19.4053	1.6	91.2	2.0	78.8	6
D	272.5892	-19.5053	3.0	18.3	2.0	28.3	5
D	272.5539	-19.5053	3.2	36.7	2.3	46.7	6
D	272.4832	-19.5053	1.6	48.9	2.7	58.9	6
D	272.4479	-19.4387	2.0	52.2	2.1	62.2	3
D	272.4833	-19.4053	1.6	37.0	2.1	47.0	6

The absolute difference between mean orientation of polarisation in each cell and the filament orientation is presented in the column of $|\langle \theta_{PA} \rangle - \theta_{\text{filament}}|$. The number of starlight polarisation in each cell is listed in the column of N_{pol} .

of $> 267 \pm 26 \mu\text{G}$ for the dense condensation in region C (the rectangle in Figures 3 and 4). In the envelope of G11, the gas density is much lower than that in the spine. Assuming energy equipartition between turbulence and perturbed magnetic fields, given by

$$\frac{1}{2}\rho\delta v^2 \sim \frac{\delta B^2}{8\pi}, \quad (5)$$

the polarisation angle dispersion, $\delta\phi \approx \frac{\delta B}{B}$, yields the Davis-Chandrasekhar-Fermi (DCF) method (Davis & Greenstein 1951; Chandrasekhar & Fermi 1953) for estimating the on-sky strength of

magnetic field

$$B_{\text{sky}} = Q\sqrt{4\pi\rho}\frac{\delta v}{\delta\phi}, \quad (6)$$

where Q is the correction factor, ρ is the gas density, and δv is the gas velocity dispersion.

The $^{13}\text{CO } J=1-0$ emission is mostly optically thin within the envelope of G11. The moment 2 map of $^{13}\text{CO } J=1-0$ emission provides the velocity dispersion δv of molecular gas across G11. The median δv values of the areas overlapping with starlight polarisation are extracted from the moment 2 map of ^{13}CO emission. The den-

Table 3. The physical properties of the four regions in G11.

Region	$n(\text{H}_2)$ (10^3 cm^{-3})	δv (km s^{-1})	$\delta \phi$ ($^\circ$)	B_{sky} (μG)	v_A (km s^{-1})	\mathcal{M}_A
A	0.4	1.8	7 ± 1	108 (54)	6.3 (3.2)	0.3 (0.6)
B	0.5	1.9	20 ± 4	48 (40)	2.8 (2.3)	0.7 (0.8)
C	0.7	2.0	22 ± 3	55 (47)	3.2 (2.7)	0.6 (0.7)
D	0.8	2.1	33 ± 9	39 (42)	2.3 (2.4)	0.9 (0.9)

The field strength, Alfvén speed, and Alfvén Mach number, estimated from the DCF and ST methods are both given in the columns of B_{sky} , v_A , and \mathcal{M}_A . The ST estimates are always in the parentheses after the DCF estimates.

sity of molecular gas, or molecular hydrogen number density $n(\text{H}_2)$ multiplied by μm_{H} ($\mu = 2.83$ is the average molecular gas weight (Kauffmann et al. 2008), m_{H} is the mass of a single hydrogen atom), is always a challenging task in characterizing the fundamental properties of molecular clouds. The mean gas density of G11 was estimated to be as $n(\text{H}_2) \approx 0.5 \times 10^3 \text{ cm}^{-3}$ at a scale of ~ 5 pc (see Fig.4 in Kainulainen et al. 2013). Assuming the LOS extent ~ 5 pc for the envelope of G11, $n(\text{H}_2)$ is approximately $N(\text{H}_2)/5$ pc, where $N(\text{H}_2)$ is the hydrogen column density derived from $^{13}\text{CO } J=1-0$ emission. The median $n(\text{H}_2)$ of region A is $0.4 \times 10^3 \text{ cm}^{-3}$, roughly consistent with the large scale $n(\text{H}_2) \approx 0.5 \times 10^3 \text{ cm}^{-3}$ in Kainulainen et al. (2013).

The starlight polarisation orientations show ordered mean orientation in the four regions of the G11 filament, an indication of ordered magnetic fields. Therefore, the polarisation angle dispersion $\delta \phi$ due to turbulence can be determined from the angular dispersion function (ADF; Falceta-Gonçalves et al. 2008; Hildebrand et al. 2009; Houde et al. 2009). The ADF method obtains a measure of the difference in polarisation angle of $N(l)$ pairs of starlight polarisation separated by displacement l (Hildebrand et al. 2009):

$$\langle \Delta \Phi^2(l) \rangle^{1/2} = \left\{ \frac{1}{N(l)} \sum_{i=1}^{N(l)} [\Phi(x) - \Phi(x+l)]^2 \right\}^{1/2}. \quad (7)$$

The polarisation angle dispersion attributed to the turbulent magnetic field, $B_t(x)$, and the large scale structure magnetic field, $B_0(x)$, are folded into the $\langle \Delta \Phi^2(l) \rangle^{1/2}$. If the large scale and turbulent magnetic fields are statistically independent, and the turbulent dispersion of polarisation angle is a constant b for the displacement l larger than the turbulent correlation length δ , characterizing $B_t(x)$, the following equation holds

$$\langle \Delta \Phi^2(l) \rangle_{\text{tot}} \approx b^2 + m^2 l^2 + \sigma_M^2(l), \quad (8)$$

when $\delta < l \ll d$, where d is the typical scale length of variations in $B_0(x)$, and $\sigma_M(l)$ is the measurement uncertainty (Hildebrand et al. 2009). Houde et al. (2009) obtained a turbulent correlation length $\delta \approx 0.016$ pc for the massive star-forming cloud OMC-1 at a distance of 450 pc. Following the same method as Houde et al. (2009), Franco et al. (2010) estimated the turbulent correlation length δ to be of a few 0.001 pc for the Pipe nebula at a distance of 145 pc. For the G11 filament, at a distance of 3.6 kpc, the closest separation between any pair of starlight polarisation is ≈ 0.1 pc, at least one order of magnitude higher than the turbulent correlation length δ found for OMC-1 cloud and Pipe nebula. The length of G11 is about 30 pc and the sizes of regions A, B, C and D are ≥ 6 pc. The starlight polarisation towards G11 satisfies the condition $\delta \ll l \ll d$, which implies that Equation 8 is suitable for deriving the turbulent dispersion of polarisation angle.

Figure 6 shows the ADF of the four regions along with the best fit

from Equation 8 using the first five data points ($l \leq 2.5$ or ≤ 2.6 pc). The constant b is determined by the zero intercept of the best fit to the ADF, at $l = 0$. According to the work by Houde et al. (2009), the ratio of turbulent to large scale magnetic fields is a function of the constant b :

$$\frac{\langle B_t^2 \rangle^{1/2}}{B_0} = \frac{b}{\sqrt{2 - b^2}}. \quad (9)$$

We use δB to replace $\langle B_t^2 \rangle^{1/2}$, and define the polarisation angle dispersion as $\delta \phi = \frac{\delta B}{B_0}$. Table 3 shows the results of ADF analyses of the four regions in G11.

We utilize the $\delta \phi$ obtained from the ADF analyses to estimate the strength of B_{sky} in the four regions. MHD simulations found that the original DCF method would overestimate the field strength. Therefore, a correction factor, Q in Equation 6, was proposed to bring the field strength derived from the DCF method closer to the model field strength (Ostriker et al. 2001; Heitsch et al. 2001). For the ordered magnetic fields with $\delta \phi < 25^\circ$, $Q \approx 0.5$ yields a reasonable estimate on the field strength (Ostriker et al. 2001; Heitsch et al. 2001). For regions C and D with $\delta \phi \geq 25^\circ$, we still assume $Q \approx 0.5$, but the field strength within them is quite uncertain. From Equation 6, we estimate the B_{sky} strength of the four regions in G11. We present the B_{sky} strength estimated from the DCF method, and the corresponding Alfvén speed v_A and Alfvén Mach number \mathcal{M}_A in Table 3 for the four regions.

The DCF method is based on the assumption that turbulence is sub-Alfvénic. MHD simulations demonstrated that the field strength obtained by the DCF method is reliable when molecular gas is sub-Alfvénic or equivalently $\delta \phi < 25^\circ$ (Ostriker et al. 2001; Falceta-Gonçalves et al. 2008; Liu et al. 2021). The field lines close to the LOS would cause large polarisation angle dispersion even if the turbulence is sub-Alfvénic (Falceta-Gonçalves et al. 2008). The polarisation angle dispersion, $\delta \phi$, is smallest in region A. The highly ordered starlight polarisation in region A implies that magnetic fields in region A are close to the plane of the sky. The projection effect due to the field orientation is small in region A. The field strength in region A, estimated from the DCF method, is $108 \mu\text{G}$, while much lower field strength is found in regions B, C, and D.

Skalidis & Tassis (2021) proposed a new method for estimating magnetic field strength in the compressible ISM. Unlike the DCF method assuming the cross term $\delta B \cdot B_0 = 0$, Skalidis & Tassis (2021) included this cross term, and assumed the turbulent kinetic energy equal to the magnetic energy fluctuations. They obtained

$$\frac{1}{2} \rho \delta v^2 = \frac{\delta B B_0}{4\pi}, \quad (10)$$

and the new method (hereafter ST) for estimating magnetic field

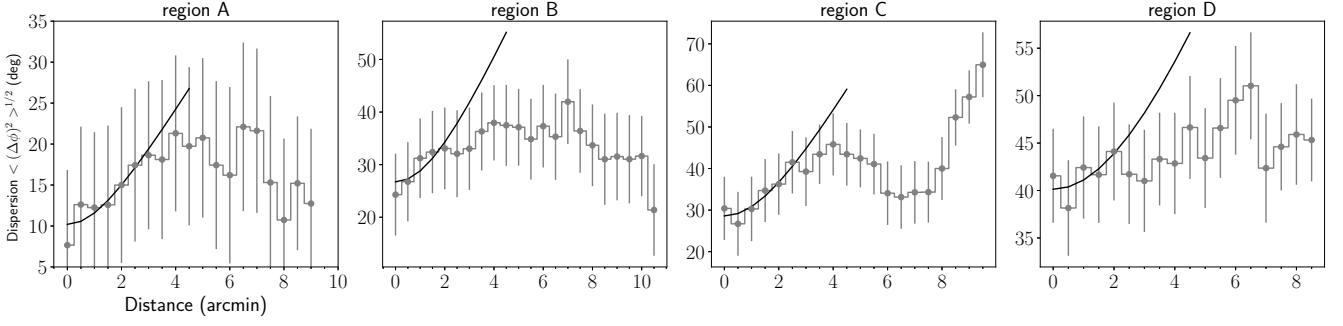


Figure 6. The angular dispersion function vs. displacement distance of the four regions in G11. The solid line represents the best fit to the ADF of the four regions. The measurement uncertainties were subtracted prior to computing the fits to the data.

strength

$$B_{\text{sky}} = \sqrt{2\pi\rho} \frac{\delta v}{\sqrt{\delta\phi}}. \quad (11)$$

Although the polarisation angle dispersion $\delta\phi$ is caused by the perpendicular fluctuations of magnetic energy rather than the parallel fluctuations, Skalidis et al. (2021) demonstrated that perpendicular fluctuations are comparable to the parallel fluctuations, thus $\delta\phi$ can also be utilized in the ST method. The magnetic field strength in the four regions, estimated by the ST method, are given in the parentheses after the DCF estimates in Table 3. The field strength estimated by the ST method is lower than that by the DCF method. The reduction factor is nearly two for region A, in which $\delta\phi$ is small. In regions B, C, and D with much higher $\delta\phi$ and higher density, the ST method returns field strength comparable to the DCF estimates. In contrast to the DCF method, the square root of $\delta\phi$ used in the ST method will weaken the effect of $\delta\phi$ variation on calculating the magnetic field strength. The ST method derives rather constant field strength, about $50 \mu\text{G}$, for the four regions.

With the field strength estimated from the DCF or ST method, v_A in the four regions are computed using $v_A = |B_{\text{sky}}|/\sqrt{4\pi\rho}$. Table 3 lists the v_A from the DCF and ST methods. The Alfvénic Mach number \mathcal{M} is a function of the polarisation angle dispersion $\delta\phi$, depending on the DCF or ST method. Following the DCF method, $\mathcal{M}_A = \frac{\delta\phi}{Q}$, depends only on $\delta\phi$ when the correction factor $Q \approx 0.5$ is fixed. Note that the ST method derives $\mathcal{M}_A = \sqrt{2\delta\phi}$, higher than that derived from the DCF method. For instance, \mathcal{M}_A of region A estimated from the ST method is 0.6, twice that estimated from the DCF method. The difference in \mathcal{M}_A between the two methods is small for regions B, C, and D. The turbulence within the four regions of G11 is generally sub-Alfvénic to trans-Alfvénic. If the turbulence is super-Alfvénic, the isotropic turbulence would twist the field lines. The average field orientations traced by starlight polarisation would be close to random distribution, and the average starlight polarisation degree is likely to be small. The average starlight polarisation per cell (see Table 2) is aligned perpendicular to the G11 filament, and the average polarisation degree per cell is typically 2-3%. The turbulence within G11 is sub-Alfvénic to trans-Alfvénic, indicating that magnetic fields are generally more important than, or as important as, turbulence.

4 DISCUSSION

4.1 Sub-Alfvénic to trans-Alfvénic envelope

The starlight polarisation within the $2' \times 2'$ grid spacing across G11, in principle, provides the information about the \mathcal{M}_A distribution across G11. Figure 4 shows the map of polarisation angle dispersion $\delta\phi$ with a grid spacing of $2' \times 2'$. The \mathcal{M}_A map, derived from $\mathcal{M}_A = \frac{\delta\phi}{0.5}$ following the DCF method, is shown in the top panel of Figure 7. In region A, the \mathcal{M}_A values obtained from the ST method are roughly twice the values from the DCF method; in regions B, C, and D, the \mathcal{M}_A values obtained from both methods are overall consistent (see also Table 3). The \mathcal{M}_A distributions across G11 is sub-Alfvénic to trans-Alfvénic, an indication that magnetic field channels the gas flow from the envelope to the spine of G11. To better explore the gas flow from the envelope to the spine, we present the moment 1 map from the $^{13}\text{CO } J=1-0$ emission along with magnetic fields in Figure 8. The moment 0 and moment 2 maps of $^{13}\text{CO } J=1-0$ emission are shown in Figures A1 and A2 in Appendix A. In region A the gas velocity is fairly uniform, indicating little velocity gradient along the LOS. The magnetic fields in region A are likely oriented on the plane of the sky, implied by the highly aligned starlight polarisation in region A. Such oriented magnetic fields channel gas flow from the envelope to the spine without producing observable velocity gradient along LOS, which is consistent with the uniform velocity field in region A. Different from region A, the LOS components of magnetic fields in region B might be more pronounced. The gas flow along the LOS components of magnetic fields from the envelope to the spine in region B would lead to observable velocity gradient perpendicular to the spine. The gas flow from the envelope in both side onto the spine in middle would cause red-shifted and blue-shifted components relative to the gas velocity in the spine. In Figure 8 we note the 32 km s^{-1} area roughly parallel to spine, the area with velocity below 31 km s^{-1} on the opposite site, and the spine with velocity in between $31 - 32 \text{ km s}^{-1}$. The blue-shifted and red-shifted areas on the two sides of the spine in region B suggest that gas flow from the envelope onto the spine is threaded by the magnetic fields.

4.2 Mass-to-flux ratio distribution

The critical mass-to-flux ratio for the magnetic stability, $(M/\Phi)_{\text{crit}} = \frac{1}{2\pi\sqrt{G}}$, is given by Nakano & Nakamura (1978), where G is the gravitational constant. The mass-to-flux ratio normalized by $(M/\Phi)_{\text{crit}}$ is evaluated as follows

$$\lambda = \frac{M/\Phi}{(M/\Phi)_{\text{crit}}} = 2\pi\sqrt{G}\mu m_{\text{H}} \frac{N(\text{H}_2)}{B_{\text{sky}}}, \quad (12)$$

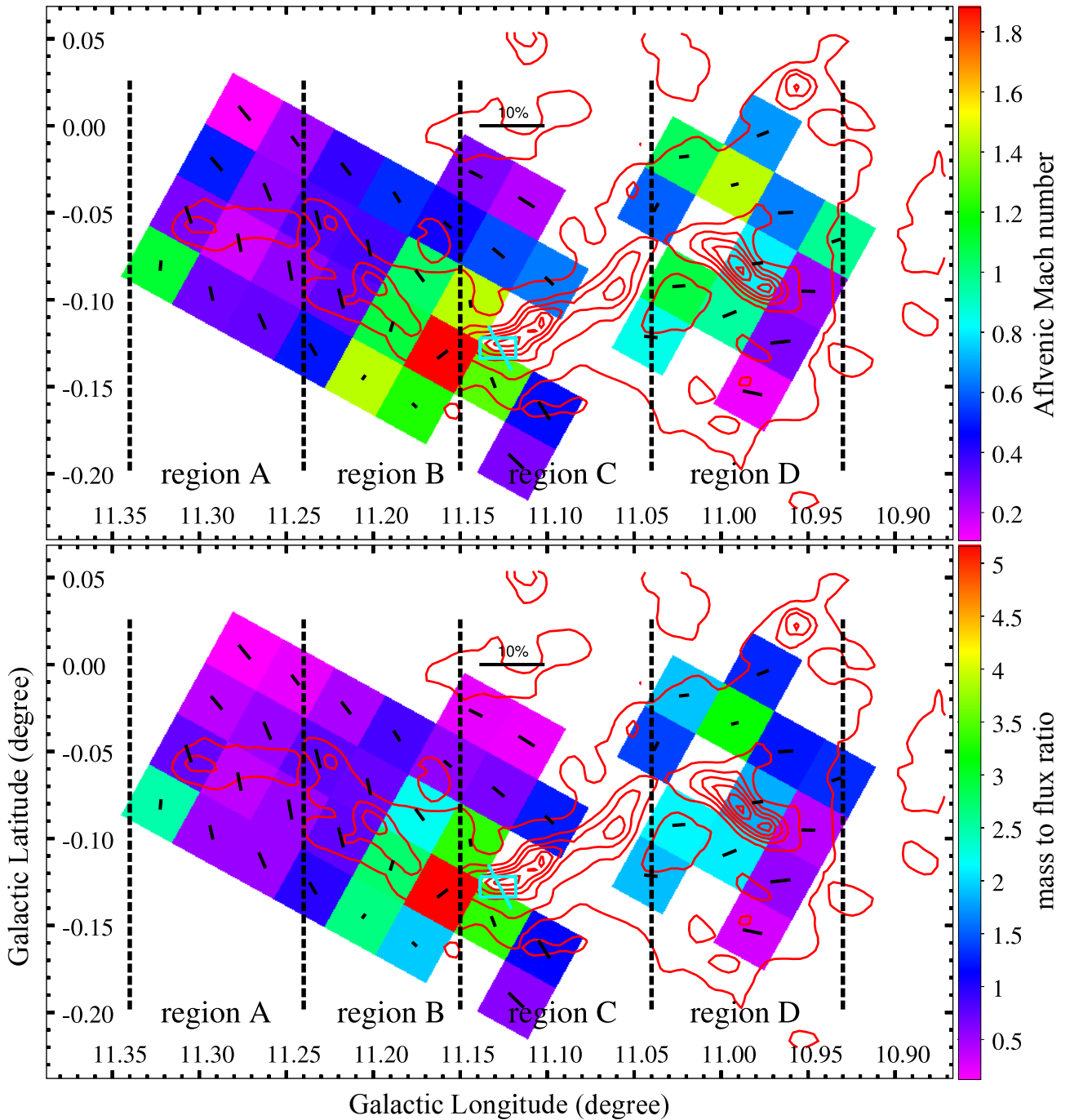


Figure 7. Alfvén Mach number map (top panel) and dimensionless λ map (bottom panel) of G11. The mean polarisation in each cell is as same as in Figure 4, but is displayed as the black segments. The red contours, cyan rectangles and segments are as same as in Figure 4.

where $\mu = 2.83$ is the average molecular gas weight (Kauffmann et al. 2008). The $N(\text{H}_2)$ map used in deriving the λ map is from the ^{13}CO $J=1-0$ emission across G11. The field strength $|B_{\text{sky}}|$ estimated from the DCF method and $N(\text{H}_2)$ maps yield the distribution of λ across G11, as shown in the bottom panel of Figure 7. We also obtained the λ distribution across G11 based on the field strength from the ST method. The two methods show consistency for λ in regions B, C, and D, in which field strengths estimated from both methods are comparable to each other (see also Table 3). The λ distributions in regions B, C, and D are mostly $\lambda \gtrsim 1$, indicative of magnetically critical envelope in these regions of G11. When the field strength of

$\sim 300 \mu\text{G}$ and an average $N(\text{H}_2)_{\text{dust}} \sim 6.5 \times 10^{22} \text{ cm}^{-2}$ are adopted for the spine of region C (Pillai et al. 2015), the λ in the spine of region C is reduced to a level of marginally supercritical, which is consistent with the λ obtained for region C in this work. The λ in region A is around 0.5 from the DCF method or close to 1 from the ST method. Moreover, the $N(\text{H}_2)$ in region A has a mean value $\sim 6 \times 10^{21} \text{ cm}^{-2}$. Both the $N(\text{H}_2)$ and λ in region A show some consistency with the MHD simulations by Seifried et al. (2020), in which the transition from parallel to perpendicular occurs at a transition column density $\approx 10^{21-21.5} \text{ cm}^{-2}$ and at a transition λ close to 1.

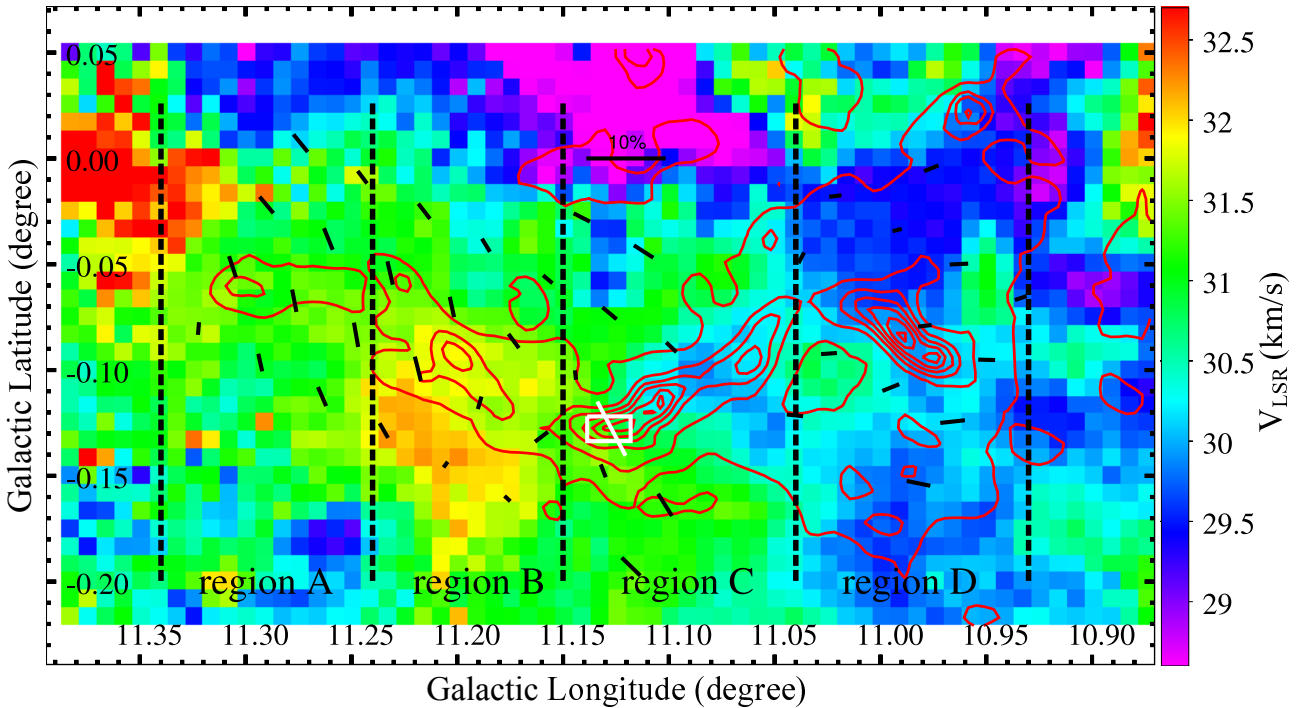


Figure 8. Moment 1 map from the $^{13}\text{CO } J=1-0$ emission in the velocity range of $25 - 37 \text{ km s}^{-1}$. The mean polarisation in each cell is as same as in Figure 4. The red contours, white rectangle and segment are as same as in Figure 3.

4.3 The role of magnetic fields in G11

The magnetic field orientations in the envelope of G11 are almost identical to that in the spine of region C (Pillai et al. 2015). This consistency between parsec scale and sub-parsec scale magnetic field orientations suggests the important role of magnetic fields in assembling the mass of G11. The field strength in the envelope of G11 is likely in the range $\sim 50 - 100 \mu\text{G}$. The median $n(\text{H}_2)$ of region A is $0.4 \times 10^3 \text{ cm}^{-3}$. Pillai et al. (2015) estimated magnetic field strength of $> 267 \pm 26 \mu\text{G}$ in the spine of region C. They adopted $n(\text{H}_2) \approx 3 \times 10^4 \text{ cm}^{-3}$ in the estimate of magnetic field strength. The density contrast between the spine and the envelope of G11 is ~ 75 . If adopting the relation $|B| \propto \rho^{0.65}$ used in Crutcher (2012), the magnetic field strength contrast between the spine and the envelope is as high as ~ 17 , much higher than the observed contrast of $\sim 3 - 5$. The observed magnetic field contrast between the spine and the envelope of G11 does not follow the nominal scaling relationship between magnetic field strength and gas density. Magnetic fields are not significantly enhanced in the spine of G11 as material is assembled onto the spine. This can be explained by gas flow guided by the field lines. Gas flow along the field lines cannot efficiently compress magnetic fields, leading to a minor enhancement of field strength when gas flows are merging onto the filament and a shallower relation $|B| \propto \rho^{0.4}$ (Li et al. 2015). For G11, we estimate both the magnetic field strength and density for the envelope, called B_{env} and ρ_{env} . Meanwhile, Pillai et al. (2015) estimate both the magnetic field strength and density for the densest part of the G11 filament, called B_{fil} and ρ_{fil} . The power index of the scaling relation can be derived by $\frac{\log B_{\text{fil}} - \log B_{\text{env}}}{\log \rho_{\text{fil}} - \log \rho_{\text{env}}}$. Adopting a field strength $B_{\text{env}} = 75 \mu\text{G}$ between the DCF and ST estimates and $\rho_{\text{env}} = 0.4 \times 10^3 \text{ cm}^{-3}$ estimated in this work, as well as $B_{\text{fil}} = 267 \mu\text{G}$ and $\rho_{\text{env}} = 3 \times 10^4 \text{ cm}^{-3}$ (Pillai et al. 2015), the field strength is proportional to $\rho^{0.3}$, similar to that measured for NGC 6334, in which the elongated gas struc-

tures at all scales are nearly perpendicular to the magnetic fields (Li et al. 2015). The flat scaling relation $|B| \propto n^{0.3}$ found for G11 suggests the important role of the magnetic fields in the formation of G11. Firstly, the dense spine can easily be formed without much magnetic field resistance. Secondly, the spine becomes magnetically supercritical, because the field strength is increasing slower than gas density. The spine could reach a high volume density, resulting in a small thermal Jeans mass that is conducive to forming low-mass stars (Li et al. 2010). The outflows, traced by high-velocity CO $J=2-1$ emission towards the dust condensation G10.99–0.08 in region D (Sanhueza et al. 2019), are mostly driven by low-mass protostars with masses below their mass sensitivity of $\sim 1 - 2 M_{\odot}$ (Pillai et al. 2019). This overabundance of low-mass protostars in the densest region D of G11, and the perpendicular magnetic fields as shown in this work, are in agreement with the predictions drawn from the MHD simulations (Li et al. 2010).

5 CONCLUSIONS

G11 is a filamentary IRDC and it is among the densest types of filaments. Its CO molecular line observations show supersonic turbulence of $\delta v \sim 2 \text{ km s}^{-1}$. Coordinated with the measurements of magnetic fields in this work, the supersonic turbulence is also sub-Alfvénic in the envelope of G11, and increases to trans-Alfvénic towards the dense regions of G11. The dynamically important magnetic fields in the envelope of G11 have general implications in the formation of dense filaments. The supersonic and sub-Alfvénic turbulence can easily compress gas along the field lines, resulting in density enhanced filament perpendicular to the field lines (Nakamura & Li 2008; Li et al. 2010). As soon as the filament becomes supercritical, global collapse starts. Gas in the envelope free-falls onto the supercritical filament. In the case of strong magnetic fields ($50 - 100 \mu\text{G}$), global collapse is more efficient along the magnetic fields, and this

results in higher density structures perpendicular to the strong magnetic fields. Barreto-Mota et al. (2021) found that gravity helps the creation of density structures perpendicular to magnetic fields in their sub-Alfvénic models. We suggest that dense filaments like G11 are more easily formed in sub-Alfvénic self-gravitating turbulent molecular clouds. Magnetic fields determine the orientation of the filaments formed in such clouds.

ACKNOWLEDGEMENTS

We would like to thank the anonymous referees for their in-depth reviews, which helped us in improving the manuscript. This work is supported by the general grant Nos. U2031202 and 11903083 of the National Natural Science Foundation of China. We are grateful to all the members of the MWISP project, for their long-term support. MWISP is sponsored by the National Key R&D Program of China with grant No. 2017YFA0402700 and the CAS Key Research Program of Frontier Sciences with grant No. QYZDJ-SSW-SLH047. This paper uses observations made at the South African Astronomical Observatory (SAAO). We thank the SAAO support astronomers and previous observer of the IRSF telescope for their technical support during the observation nights at Sutherland, South Africa, and the SAAO staff members for taking care of our lives at the SAAO. This work has made use of data from the European Space Agency (ESA) mission *Gaia* (<https://www.cosmos.esa.int/gaia>), processed by the *Gaia* Data Processing and Analysis Consortium (DPAC, <https://www.cosmos.esa.int/web/gaia/dpac/consortium>). Funding for the DPAC has been provided by national institutions, in particular the institutions participating in the *Gaia* Multilateral Agreement. This work has made use of 353 GHz dust polarisation data, based on observations obtained with Planck (<http://www.esa.int/Planck>), an ESA science mission with instruments and contributions directly funded by ESA Member States, NASA, and Canada. This work has made use of NASA's Astrophysics Data System. This research is based on data products from observations made with ESO Telescopes at the La Silla or Paranal Observatories under ESO programme ID 179.B-2002, and has made use of the services of the ESO Science Archive Facility.

We use *Python* packages NUMPY (Harris et al. 2020), SCIPY (Virtanen et al. 2020), ASTROPY (Astropy Collaboration et al. 2013, 2018), and Spectral-cube (Ginsburg et al. 2015) to analyse the data used in this work. We use SAOImage DS9 (Joye & Mandel 2003; Joye 2019) and *Python* package MATPLOTLIB (Hunter 2007) for data visualization.

DATA AVAILABILITY

The full version of Table 1 and MWISP CO data of G11 are available in <https://www.scidb.cn/en>, at <https://dx.doi.org/10.57760/sciencedb.01942> (Chen et al. 2022a).

REFERENCES

- Andersson B.-G., Lazarian A., Vaillancourt J. E., 2015, *ARA&A*, 53, 501
- André P., Di Francesco J., Ward-Thompson D., Inutsuka S. I., Pudritz R. E., Pineda J. E., 2014, in Beuther H., Klessen R. S., Dullemond C. P., Henning T., eds, *Protostars and Planets VI*. p. 27 ([arXiv:1312.6232](https://arxiv.org/abs/1312.6232)), [doi:10.2458/azu_uapress_9780816531240-ch002](https://doi.org/10.2458/azu_uapress_9780816531240-ch002)
- Arthur S. J., Henney W. J., Mellema G., de Colle F., Vázquez-Semadeni E., 2011, *MNRAS*, 414, 1747
- Arzoumanian D., et al., 2021, *A&A*, 647, A78
- Astropy Collaboration et al., 2013, *A&A*, 558, A33
- Astropy Collaboration et al., 2018, *AJ*, 156, 123
- Bailer-Jones C. A. L., Rybizki J., Foesneau M., Demleitner M., Andrae R., 2021, *AJ*, 161, 147
- Barreto-Mota L., de Gouveia Dal Pino E. M., Burkhart B., Melioli C., Santos-Lima R., Kadowaki L. H. S., 2021, *MNRAS*, 503, 5425
- Beuther H., et al., 2014, *A&A*, 571, A53
- Carey S. J., Clark F. O., Egan M. P., Price S. D., Shipman R. F., Kuchar T. A., 1998, *ApJ*, 508, 721
- Carey S. J., Feldman P. A., Redman R. O., Egan M. P., MacLeod J. M., Price S. D., 2000, *ApJ*, 543, L157
- Chandrasekhar S., Fermi E., 1953, *ApJ*, 118, 113
- Chapman N. L., Goldsmith P. F., Pineda J. L., Clemens D. P., Li D., Krčo M., 2011, *ApJ*, 741, 21
- Chen Z., Jiang Z., Wang Y., Chini R., Tamura M., Nagayama T., Nagata T., Nakajima Y., 2012, *PASJ*, 64, 110
- Chen Z., Nürnberger D. E. A., Chini R., Liu Y., Fang M., Jiang Z., 2013, *A&A*, 557, A51
- Chen C.-Y., King P. K., Li Z.-Y., 2016, *ApJ*, 829, 84
- Chen Z., Jiang Z., Tamura M., Kwon J., Roman-Lopes A., 2017, *ApJ*, 838, 80
- Chen C.-Y., et al., 2020, *MNRAS*, 494, 1971
- Chen Z., Sefako R., Yang Y., Jiang Z., Su Y., Zhang S., Zhou X., 2022a, *Strong Magnetic Fields Play Important Role in the Filamentary Infrared Dark Cloud G11.11-0.12*, [doi:10.57760/sciencedb.01942](https://doi.org/10.57760/sciencedb.01942), <https://doi.org/10.57760/sciencedb.01942>
- Chen Z., Sefako R., Yang Y., Jiang Z., Yu S., Yin J., 2022b, *Research in Astronomy and Astrophysics*, 22, 075017
- Clark S. E., Peek J. E. G., Putman M. E., 2014, *ApJ*, 789, 82
- Clemens D. P., Pinnick A. F., Pavel M. D., Taylor B. W., 2012, *ApJS*, 200, 19
- Clemens D. P., Pavel M. D., Cashman L. R., 2013, *AJ*, 145, 74
- Clemens D. P., et al., 2020, *ApJS*, 249, 23
- Crutcher R. M., 2012, *ARA&A*, 50, 29
- Davis J. L., Greenstein J. L., 1951, *ApJ*, 114, 206
- Devaraj R., Clemens D. P., Dewangan L. K., Luna A., Ray T. P., Mackey J., 2021, *ApJ*, 911, 81
- Doi Y., et al., 2020, *ApJ*, 899, 28
- Eswaraiah C., et al., 2019, *ApJ*, 875, 64
- Eswaraiah C., et al., 2021, *ApJ*, 912, L27
- Falceta-Gonçalves D., Lazarian A., Kowal G., 2008, *ApJ*, 679, 537
- Fiege J. D., Johnstone D., Redman R. O., Feldman P. A., 2004, *ApJ*, 616, 925
- Fissel L. M., et al., 2019, *ApJ*, 878, 110
- Franco G. A. P., Alves F. O., Girart J. M., 2010, *ApJ*, 723, 146
- Gaia* Collaboration et al., 2016, *A&A*, 595, A1
- Gaia* Collaboration et al., 2021, *A&A*, 649, A1
- Gehman C. S., Adams F. C., Watkins R., 1996, *ApJ*, 472, 673
- Ginsburg A., et al., 2015, in Iono D., Tatematsu K., Wootten A., Testi L., eds, *Astronomical Society of the Pacific Conference Series Vol. 499, Revolution in Astronomy with ALMA: The Third Year*. pp 363–364
- Goldsmith P. F., Heyer M., Narayanan G., Snell R., Li D., Brunt C., 2008, *ApJ*, 680, 428
- Gómez G. C., Vázquez-Semadeni E., 2014, *ApJ*, 791, 124
- Gómez L., Wyrowski F., Pillai T., Leurini S., Menten K. M., 2011, *A&A*, 529, A161
- Gómez G. C., Vázquez-Semadeni E., Zamora-Avilés M., 2018, *MNRAS*, 480, 2939
- Greaves J. S., et al., 2003, *MNRAS*, 340, 353
- Hacar A., Clark S., Heitsch F., Kainulainen J., Panopoulou G., Seifried D., Smith R., 2022, *arXiv e-prints*, [p. arXiv:2203.09562](https://arxiv.org/abs/2203.09562)
- Hanawa T., et al., 1993, *ApJ*, 404, L83
- Harris C. R., et al., 2020, *Nature*, 585, 357
- Heitsch F., Zweibel E. G., Mac Low M.-M., Li P., Norman M. L., 2001, *ApJ*, 561, 800
- Heitsch F., Slyz A. D., Devriendt J. E. G., Hartmann L. W., Burkert A., 2006, *ApJ*, 648, 1052
- Heitsch F., Stone J. M., Hartmann L. W., 2009, *ApJ*, 695, 248

- Hennebelle P., 2013, *A&A*, **556**, A153
- Henning T., Linz H., Krause O., Ragan S., Beuther H., Launhardt R., Nielbock M., Vasyunina T., 2010, *A&A*, **518**, L95
- Heyer M., Soler J. D., Burkhardt B., 2020, *MNRAS*, **496**, 4546
- Hildebrand R. H., Kirby L., Dotson J. L., Houde M., Vaillancourt J. E., 2009, *ApJ*, **696**, 567
- Houde M., Vaillancourt J. E., Hildebrand R. H., Chitsazzadeh S., Kirby L., 2009, *ApJ*, **706**, 1504
- Hull C. L. H., Plambeck R. L., 2015, *Journal of Astronomical Instrumentation*, **4**, 1550005
- Hunter J. D., 2007, *Computing in Science and Engineering*, **9**, 90
- Ibáñez-Mejía J. C., Mac Low M.-M., Klessen R. S., 2022, *ApJ*, **925**, 196
- Inoue T., Inutsuka S.-i., 2008, *ApJ*, **687**, 303
- Johnstone D., Fiege J. D., Redman R. O., Feldman P. A., Carey S. J., 2003, *ApJ*, **588**, L37
- Joye W., 2019, SAOImageDS9/SAOImageDS9 v8.0.1, Zenodo, doi:10.5281/zenodo.2530958
- Joye W. A., Mandel E., 2003, in Payne H. E., Jedrzejewski R. I., Hook R. N., eds, *Astronomical Society of the Pacific Conference Series Vol. 295*, *Astronomical Data Analysis Software and Systems XII*, p. 489
- Kainulainen J., Ragan S. E., Henning T., Stutz A., 2013, *A&A*, **557**, A120
- Kandori R., et al., 2006, in *Society of Photo-Optical Instrumentation Engineers (SPIE) Conference Series*, p. 626951, doi:10.1117/12.670967
- Kauffmann J., Bertoldi F., Bourke T. L., Evans N. J. I., Lee C. W., 2008, *A&A*, **487**, 993
- Körtgen B., Banerjee R., 2015, *MNRAS*, **451**, 3340
- Körtgen B., Soler J. D., 2020, *MNRAS*, **499**, 4785
- Krumholz M. R., Stone J. M., Gardiner T. A., 2007, *ApJ*, **671**, 518
- Lazarian A., Hoang T., 2007, *MNRAS*, **378**, 910
- Lee D., et al., 2021, *ApJ*, **918**, 39
- Li P. S., Klein R. I., 2019, *MNRAS*, **485**, 4509
- Li Z.-Y., Wang P., Abel T., Nakamura F., 2010, *ApJ*, **720**, L26
- Li H.-b., Fang M., Henning T., Kainulainen J., 2013, *MNRAS*, **436**, 3707
- Li H. B., Goodman A., Sridharan T. K., Houde M., Li Z. Y., Novak G., Tang K. S., 2014, in *Beuther H., Klessen R. S., Dullemond C. P., Henning T., eds, Protostars and Planets VI*, p. 101 (arXiv:1404.2024), doi:10.2458/azu_uapress_9780816531240-ch005
- Li H.-B., et al., 2015, *Nature*, **520**, 518
- Li S., et al., 2020, *ApJ*, **903**, 119
- Li P. S., Lopez-Rodriguez E., Ajeddig H., André P., McKee C. F., Rho J., Klein R. I., 2022, *MNRAS*, **510**, 6085
- Lin Y., et al., 2017, *ApJ*, **840**, 22
- Liu J., Zhang Q., Commerçon B., Valdivia V., Maury A., Qiu K., 2021, *ApJ*, **919**, 79
- Malinen J., et al., 2016, *MNRAS*, **460**, 1934
- Minniti D., et al., 2010, *New Astron.*, **15**, 433
- Mocz P., Burkhardt B., 2018, *MNRAS*, **480**, 3916
- Nagayama T., et al., 2003, in *M. Iye & A. F. M. Moorwood ed., Society of Photo-Optical Instrumentation Engineers (SPIE) Conference Series Vol. 4841*, *Society of Photo-Optical Instrumentation Engineers (SPIE) Conference Series*, pp 459–464, doi:10.1117/12.460770
- Naghizadeh-Khouei J., Clarke D., 1993, *A&A*, **274**, 968
- Nakamura F., Li Z.-Y., 2008, *ApJ*, **687**, 354
- Nakano T., Nakamura T., 1978, *PASJ*, **30**, 671
- Naranjo-Romero R., Vázquez-Semadeni E., Loughnane R. M., 2022, *MNRAS*, **512**, 4715
- Ostriker E. C., Stone J. M., Gammie C. F., 2001, *ApJ*, **546**, 980
- Padoan P., Juvella M., Goodman A. A., Nordlund Å., 2001, *ApJ*, **553**, 227
- Pecaat M. J., Mamajek E. E., 2013, *ApJS*, **208**, 9
- Peretto N., Fuller G. A., 2009, *A&A*, **505**, 405
- Pillai T., Wyrowski F., Menten K. M., Krügel E., 2006, *A&A*, **447**, 929
- Pillai T., Kauffmann J., Tan J. C., Goldsmith P. F., Carey S. J., Menten K. M., 2015, *ApJ*, **799**, 74
- Pillai T., Kauffmann J., Zhang Q., Sanhueza P., Leurini S., Wang K., Sridharan T. K., König C., 2019, *A&A*, **622**, A54
- Pillai T. G. S., et al., 2020, *Nature Astronomy*, **4**, 1195
- Planck Collaboration et al., 2011, *A&A*, **536**, A1
- Planck Collaboration et al., 2015, *A&A*, **576**, A104
- Planck Collaboration et al., 2016a, *A&A*, **586**, A135
- Planck Collaboration et al., 2016b, *A&A*, **586**, A138
- Ragan S., et al., 2012, *A&A*, **547**, A49
- Ragan S. E., Henning T., Beuther H., Linz H., Zahorecz S., 2015, *A&A*, **573**, A119
- Rosero V., et al., 2014, *ApJ*, **796**, 130
- Rygl K. L. J., Wyrowski F., Schuller F., Menten K. M., 2010, *A&A*, **515**, A42
- Sanhueza P., et al., 2019, *ApJ*, **886**, 102
- Santos F. P., Busquet G., Franco G. A. P., Girart J. M., Zhang Q., 2016, *ApJ*, **832**, 186
- Schneider N., et al., 2015, *A&A*, **578**, A29
- Seifried D., Walch S., 2015, *MNRAS*, **452**, 2410
- Seifried D., Walch S., Weis M., Reissl S., Soler J. D., Klessen R. S., Joshi P. R., 2020, *MNRAS*, **497**, 4196
- Serkowski K., Mathewson D. S., Ford V. L., 1975, *ApJ*, **196**, 261
- Shipman R. F., van der Tak F. F. S., Wyrowski F., Herpin F., Frieswijk W., 2014, *A&A*, **570**, A51
- Simon R., Jackson J. M., Rathborne J. M., Chambers E. T., 2006, *ApJ*, **639**, 227
- Skalidis R., Tassis K., 2021, *A&A*, **647**, A186
- Skalidis R., Sternberg J., Beattie J. R., Pavlidou V., Tassis K., 2021, *A&A*, **656**, A118
- Soler J. D., 2019, *A&A*, **629**, A96
- Soler J. D., Hennebelle P., Martin P. G., Miville-Deschênes M. A., Netterfield C. B., Fissel L. M., 2013, *ApJ*, **774**, 128
- Soler J. D., et al., 2016, *A&A*, **596**, A93
- Soler J. D., et al., 2017, *A&A*, **603**, A64
- Su Y., et al., 2019, *ApJS*, **240**, 9
- Sugitani K., et al., 2011, *ApJ*, **734**, 63
- Tafoya D., et al., 2021, *ApJ*, **913**, 131
- Tremblin P., et al., 2014, *A&A*, **564**, A106
- Vázquez-Semadeni E., 1994, *ApJ*, **423**, 681
- Vázquez-Semadeni E., Ryu D., Passot T., González R. F., Gazol A., 2006, *ApJ*, **643**, 245
- Virtanen P., et al., 2020, *Nature Methods*, **17**, 261
- Wang K., et al., 2014, *MNRAS*, **439**, 3275
- Wardle J. F. C., Kronberg P. P., 1974, *ApJ*, **194**, 249
- Wareing C. J., Falle S. A. E. G., Pittard J. M., 2019, *MNRAS*, **485**, 4686
- Whittet D. C. B., Martin P. G., Hough J. H., Rouse M. F., Bailey J. A., Axon D. J., 1992, *ApJ*, **386**, 562
- Yang Y., Jiang Z.-B., Chen Z.-W., Zhang S.-B., Yu S.-L., Ao Y.-P., 2020, *Research in Astronomy and Astrophysics*, **20**, 115
- Yang Y., Jiang Z., Chen Z., Ao Y., Yu S., 2021, *ApJ*, **922**, 144
- Zamora-Avilés M., Vázquez-Semadeni E., Körtgen B., Banerjee R., Hartmann L., 2018, *MNRAS*, **474**, 4824
- Zhang Q., et al., 2014, *ApJ*, **792**, 116
- Zhang M., Kainulainen J., Mattern M., Fang M., Henning T., 2019, *A&A*, **622**, A52

APPENDIX A: $^{13}\text{CO } J=1-0$ MOMENT 0 AND MOMENT 2 MAPS OF THE G11 FILAMENT

The moment 0 and moment 2 maps of the $^{13}\text{CO } J=1-0$ emission in the velocity range of $25 - 37 \text{ km s}^{-1}$ are shown in Figures A1 and A2, respectively.

This paper has been typeset from a \LaTeX file prepared by the author.

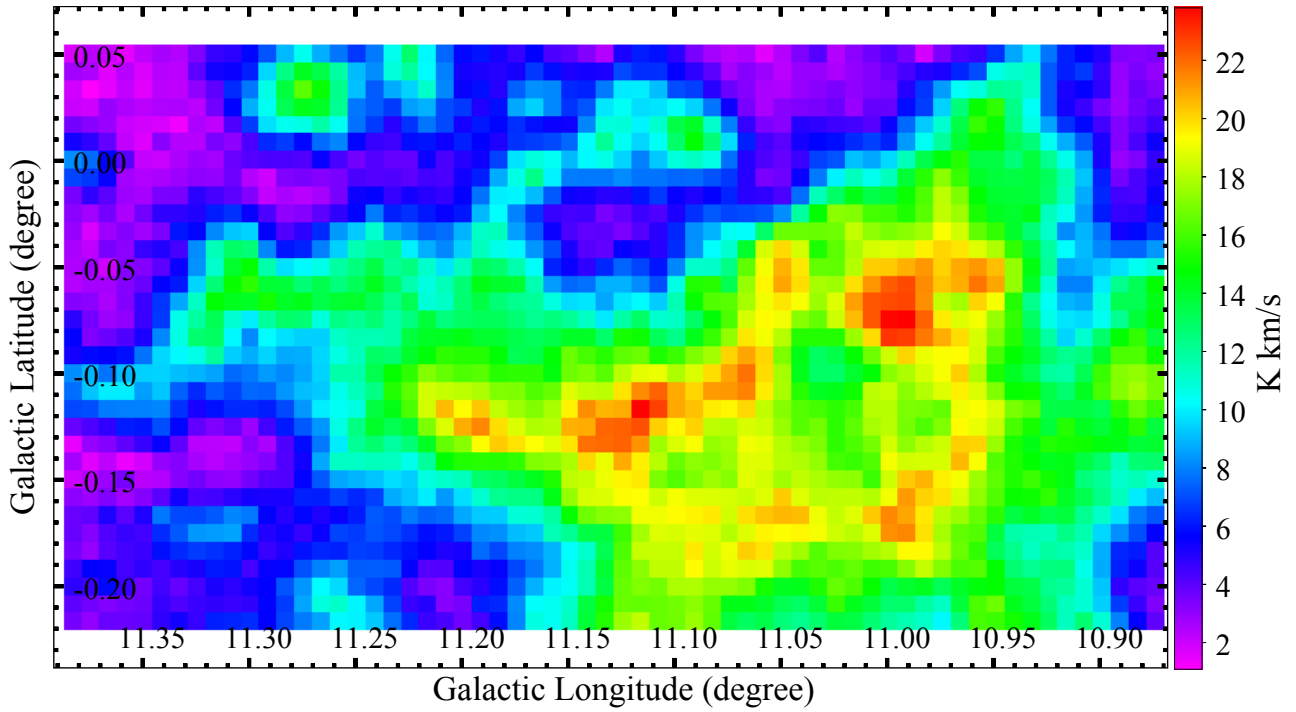


Figure A1. Moment 0 map of the $^{13}\text{CO } J=1-0$ emission in the velocity range of $25 - 37 \text{ km s}^{-1}$.

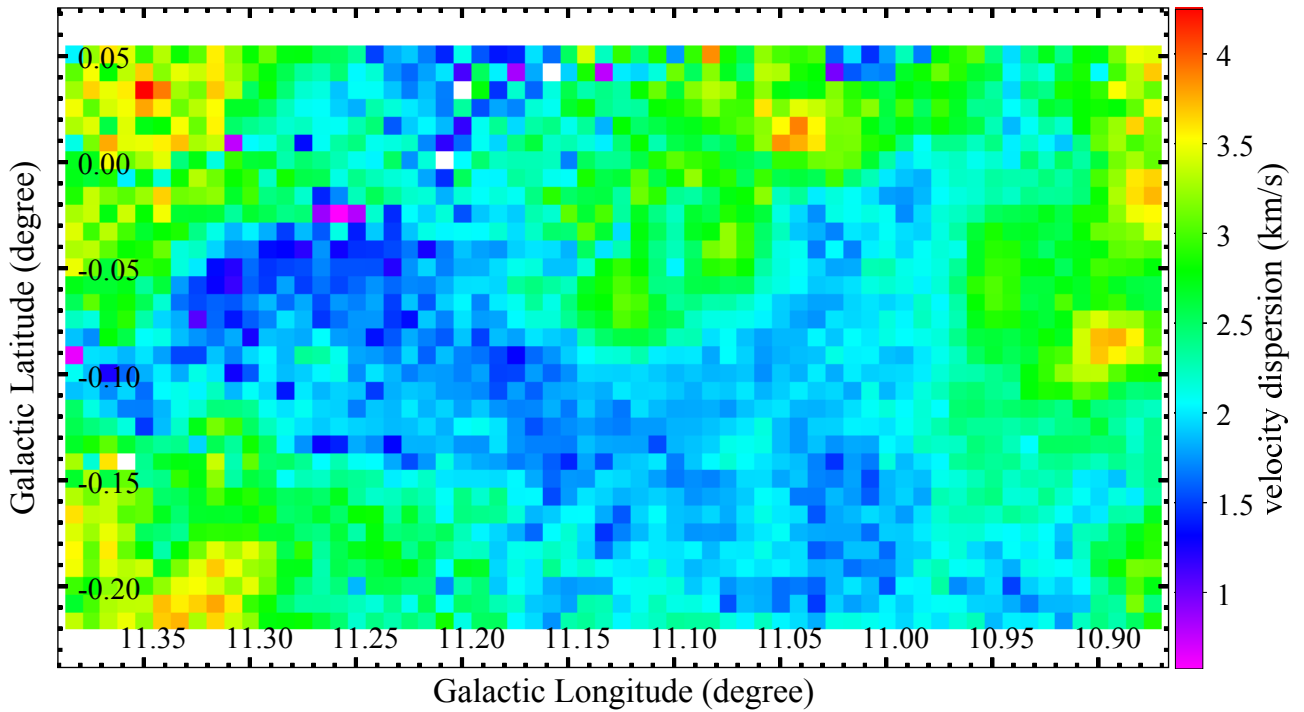


Figure A2. Moment 2 map of the $^{13}\text{CO } J=1-0$ emission in the velocity range of $25 - 37 \text{ km s}^{-1}$.